

## Research paper

# Characteristics and origin of the major authigenic minerals and their impacts on reservoir quality in the Permian Wutonggou Formation of Fukang Sag, Junggar Basin, western China

Yanzhong Wang<sup>a,\*</sup>, Miruo Lin<sup>a</sup>, Kelai Xi<sup>a</sup>, Yingchang Cao<sup>a,b</sup>, Jian Wang<sup>a</sup>, Guanghui Yuan<sup>a</sup>, Muhammad Kashif<sup>a</sup>, Mingshui Song<sup>c</sup>

<sup>a</sup> School of Geosciences, China University of Petroleum, Qingdao, 266580, China

<sup>b</sup> Laboratory for Marine Mineral Resources, Qingdao National Laboratory for Marine Science and Technology, Qingdao, 266071, China

<sup>c</sup> Exploration Management Center, Shengli Oilfield Company, SINOPEC, Dongying, Shandong, 257017, China



## ARTICLE INFO

## Keywords:

Carbonate cement  
Authigenic laumontite  
Reservoir quality  
Permian  
Junggar Basin

## ABSTRACT

This research is focused on the characteristics and origin of major authigenic minerals and the influences on the reservoir quality of the Permian Wutonggou Formation sandstones in the eastern slope of Fukang Sag, Junggar Basin, Western China. Authigenic cements were observed and described from thin sections, scanning electron microscopy, fluorescence, and cathodoluminescence. The elemental concentrations of the authigenic minerals were measured by electron probe microanalysis. Additional characterizations were obtained from O and C stable isotope ratios and from the homogenization temperature of aqueous fluid inclusions. The results show that the sandstones in the Wutonggou Formation are dominated by volcanic lithic fragments. Carbonates and laumontites are the major authigenic minerals in the study area. Authigenic quartz and kaolinite can also be observed. Two types of carbonate cements are identified. The first type is calcite with yellow fluorescent hydrocarbon inclusions. The carbon and oxygen isotopes in the calcites are highly C-depleted and O-depleted. The homogenization temperatures of the aqueous fluid inclusions in the calcite cements are higher than the highest paleogeotemperatures during the burial history. Combined with the presence of authigenic fibrous illites and the illitization of kaolinites, it is determined that the precipitation of the calcites is related to the upwelling of deep fluids and was impacted by the CO<sub>2</sub> from the thermal decarboxylation of organic matters during the middle-late Jurassic. The second type is ferroan calcite with blue fluorescent hydrocarbon inclusions and higher contents of Fe, Mn, Cr, and Mg than in the calcites. The ferroan calcites in the Beisantai uplift are rich in <sup>13</sup>C (δ<sup>13</sup>C<sub>(V-PDB)</sub> values are +22.10‰ and +22.16‰). The precipitation of these ferroan calcites was impacted by the CO<sub>2</sub> from crude oil biodegradation after the late Jurassic. Two types of laumontites are identified. The first type is partially dissolved and is characterized by a high Ca/Na ratio and low Fe contents. The second type is hardly dissolved, has hydrocarbon inclusions with yellow and blue fluorescence, and is characterized by a low Ca/Na ratio and high Fe contents. The first type of laumontite was precipitated prior to hydrocarbon charging and the second type was formed after hydrocarbon charging and meteoric water leaching. The hydration of the volcanic debris provided the source materials for both types of laumontite. The authigenic quartz and kaolinite were formed by the alteration of feldspars, laumontites, and volcanic materials. The evolution of the reservoir properties was impacted by various degrees of cementation and dissolution; as a result, the reservoir quality in the Beisantai uplift was better than in the Shaqiu area.

## 1. Introduction

The rock composition and tectonic setting significantly impact the diagenesis of clastic reservoirs (Gaupp et al., 1993; Salem et al., 2000; Labaume et al., 2008; Zhong et al., 2012). The clastic reservoirs of the

Permian Wutonggou Formation in the eastern slope of Fukang Sag in the Junggar Basin are characterized by large amounts of volcanic lithic fragments (Folk, 1980) and have undergone multi-stage tectonic subsidence and uplift (Wu et al., 2012). However, little attention has been paid to the diagenesis and origin of the major authigenic minerals in

\* Corresponding author.

E-mail addresses: [wangyanzhong1980@163.com](mailto:wangyanzhong1980@163.com) (Y. Wang), [xikelai@upc.edu.cn](mailto:xikelai@upc.edu.cn) (K. Xi).

<https://doi.org/10.1016/j.marpetgeo.2018.07.008>

Received 17 November 2017; Received in revised form 8 April 2018; Accepted 9 July 2018

Available online 12 July 2018

0264-8172/ © 2018 Elsevier Ltd. All rights reserved.

this area, which results in uncertainties regarding the diagenetic evolution of the reservoirs. Our research shows that laumontite and carbonate are the major authigenic minerals in the study area. Laumontites are generally found in sandstones rich in volcanic lithic fragments and anorthites (Noh and Boles, 1993). The albitization of anorthites provides Ca ions for the precipitation of laumontites (Ghent and Miller, 1974; Merino, 1975; Yang and Qiu, 2002; Fu et al., 2010). The hydration of volcanic materials can also release Ca ions into the pore water and provide source materials for the precipitation of carbonates and laumontites (Cuadros, 1999; Marantos et al., 2007; Zhu et al., 2016). However, the necessary ions of  $\text{Ca}^{2+}$ ,  $\text{Al}^{3+}$ , and  $\text{Si}^{4+}$  for the laumontite formation can be released by volcanic material hydration during the initial burial stage and reburial stage (Noh, 1998). In this context, the determination of the origins and phases of the laumontites is complicated. The deep fluids can flow upwards along deep faults (Pitman et al., 1997; Aydin, 2000; Suchy et al., 2000; Garden et al., 2001; Sadegh et al., 2008; De Boever et al., 2011; Khalifa and Morad, 2012) and the meteoric water can also flow downwards along deep faults (Bjørlykke et al., 1989; Bjørlykke, 1993; Juhasz et al., 2002; Menzies et al., 2014; Carpentier et al., 2014; Zhou et al., 2016; Yuan et al., 2017). The external fluids migrating along the faults strikingly impact the diagenesis of clastic reservoirs. For example, unstable components, such as feldspars, debris, and laumontites adjacent to the faults can be dissolved by meteoric water and organic acids or  $\text{CO}_2$  from deep formations (Crossey et al., 1984; Duan et al., 2017; Yuan et al., 2017). In addition, authigenic kaolinite and quartz are precipitated during this process (Kim et al., 2012; Rainoldi et al., 2015; Sliwinski et al., 2016). Furthermore, deep fluids with  $\text{CO}_2$  also provide sources for carbonate cements (Chen et al., 2004; Bazargani-Guilani, 2010). Eichhubl et al. (2009) reported that the upward-migrating reduced brines caused by the Variscan orogeny promoted the calcite formation and the calcite cementation decreased with an increasing distance from the faults. However, during uplift processes, the penetration of meteoric water and the biodegradation of hydrocarbon also supplies carbon sources for carbonates (Templeton et al., 1998; Head et al., 2003), which complicates the genesis of the carbonate cements in the study area.

The main objectives of this research are 1) to identify the diagenetic characteristics of the Permian Wutonggou Formation, 2) to analyze the source and genesis of the major diagenetic minerals, and 3) to discuss the diagenetic-paragenetic sequence and the influence of the authigenic minerals on the Permian sandstones.

## 2. Geological background

The Junggar Basin is an important petroleum-bearing basin in western China (Fig. 1A and B) and is a composite stacked basin with the characteristics of a bi-layer basement that includes the Pre-Cambrian crystalline basement and the Lower Paleozoic basement (Tang et al., 1997; Yu et al., 2014). The study area is located in the eastern part of the Junggar Basin and is bounded to the east by the Jimusaer sag, to the west by the Fukang sag, to the south by the Bogeda mountain and to the north by the Shaqi uplift (Fig. 1C); the area comprises about 800 km<sup>2</sup> (Yu et al., 2014). Based on the tectonic units, the study area can be divided into the Beisantai uplift and the Shaqiu area (Fig. 1C). The Permian strata in the study area are divided from bottom to top into the Pingdiquan Formation (P<sub>2</sub>p) and the Wutonggou Formation (P<sub>3</sub>wt) (Fig. 2). The coarse-grained sediments of the Wutonggou Formation were deposited as fan deltas and braided river deltas. The Wutonggou Formation is preserved in the eastern slope of the Fukang sag but is partially eroded in the Beisantai uplift (Fig. 1D). The whole study area has undergone a similar and complex tectonic evolution (Wu et al., 2012). During the Carboniferous-Permian, the Junggar-Turpan block collided persistently with the Siberian plate and the Tarim plate, which resulted in the Kelameili and Bogda mountains uplift. During the Late Permian, the research area continued to uplift. Coarse-grained

sediments were deposited at the mountain fronts during the sedimentation of the Wutonggou Formation (Chen et al., 2001). From the Triassic to the Middle Jurassic, the tectonic activities were relatively stable. During the Middle Jurassic-Early Cretaceous, the strata in the eastern and northeastern Junggar Basin underwent extensive folding and uplift (Zhang et al., 2006), which was interpreted as the effects of the Asia-Qiangtang collision and the Asia-Lhasa collision (De Grave et al., 2007; Glorie et al., 2010; Yang et al., 2015). Subsequently, other tectonic uplift episodes occurred in the Late Cretaceous (65–135 Ma) (Zhang et al., 2006; Novikov, 2013). In the context of multi-stage tectonic movements, the Beisantai fault (Fig. 1C and D) was active until the end of the Cretaceous (Wu et al., 2012). These processes induced the strata in the Beisantai uplift to develop extremely abundant fracture/fault systems. From the Neogene to the Quaternary, the study area experienced a rapid subsidence (Wu et al., 2012) (Fig. 3). The Beisantai uplift was a low uplift that formed prior to the sedimentation of the Wutonggou Formation (Wu et al., 2003) and the thrust of the Beisantaibeifault continued to the end of the Cretaceous (Wu et al., 2012). The seismic profile also indicated that the Permian strata are superimposed on the Carboniferous strata (Wu et al., 2012). This implies that the Permian strata on the hanging wall of the Beisantaibeifault were buried shallower than the strata on the footwall all the while.

## 3. Samples and methodology

### 3.1. Database

For this study, we collected 605 rock composition samples from thin sections, 127 casting thin sections from 14 wells, 2310 measured core porosity and permeability samples, 46 bulk rock samples from 17 wells, 38 trace element samples of mudstones, and 34 crude oil density and viscosity samples from the Geological Scientific Research Institute of the PetroChina Xinjiang Oilfield Company. The crude oil at a depth of 1534–1600 m in Well DQ-3 was also collected from the same source.

### 3.2. Petro-geochemical characterization of authigenic minerals

The chromatography analysis was performed with an HP 6890/5973 gas chromatography/mass selective detector (GC/MSD) instrument equipped with an HP-5MS fused silica column (30 m × 0.25 mm i.d., film thickness 0.25 μm). The GC oven temperature for the analysis of the saturate fractions was initially held at 50 °C for 2 min, then increased to 100 °C at 20 °C/min, and finally increased to 310 °C at 3 °C/min, where it was held for 16.5 min. The burial and thermal histories of Well B-16 and Well Sha-107 were determined using the 1-D BasinMod software. The paleogeothermal gradient in the study area was obtained from Qiu et al. (2002) and Jin (2001). The erosion amount and duration of the erosion were obtained from Jin (2001) and Jing (2009).

One-hundred and seventy-three thin sections and 46 bulk rock samples were prepared for scanning electron microscopy (SEM) and cathodoluminescence (CL) observations, aqueous fluid inclusion microthermometry, micro-drilling for stable isotope analysis, and electron probe microanalysis (EPMA). The optical and fluorescence identifications were performed using a Zeiss microscope (Imaging-2M). To obtain the quantitative statistics of the cements and secondary pores, multiple microphotographs at a magnification of 50× were obtained for the thin sections to encompass the entire thin section as much as possible. Subsequently, the area of the authigenic minerals and the dissolution pores in the microphotographs was determined using Image-Pro Plus 6.0. The proportion of the area of the authigenic minerals and the dissolution pores to the total area of the microphotographs was calculated. Finally, the average values of the areal proportions were calculated as the contents of the authigenic minerals and the dissolution pores. The CL images were acquired by a CAMBRIDGE CL8200 MK5 detector on the Zeiss microscope with an acceleration voltage of 10 kV, an electric current of 250 μA, and an exposure time of 7 s at a

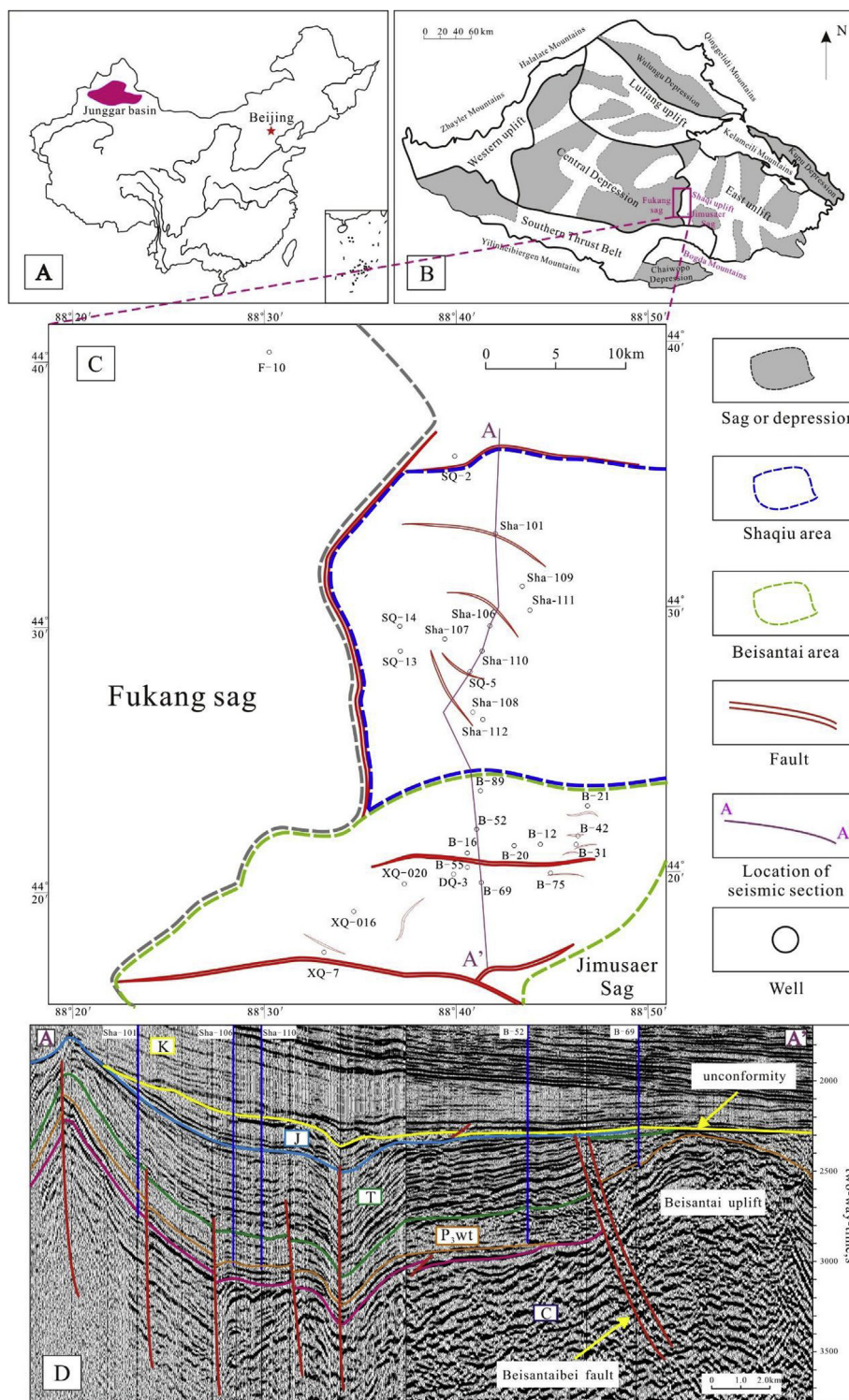


**Fig. 1.** A: The map of the Junggar Basin in the western part of China. B: Tectonic units in the Junggar Basin and the location of the research area (eastern slope of Fukang Sag). C: Structural map and the location of wells in the research area. D: The north-south seismic section (A-A') of the research area, showing the distribution of the strata and the major faults.

magnification of 100× and 14 s at a magnification of 200×. The SEM images were acquired by a Quanta200 scanning electron microscope combined with energy-dispersive X-ray spectroscopy. The microthermometric measurements of the aqueous fluid inclusions were obtained using a Linkam TH-600 stage at the China University of Petroleum. The homogenization temperature ( $T_h$ ) measurements were performed at a heating rate of 10 °C/min for temperatures lower than

70 °C, a heating rate of 5 °C/min for temperatures in the range of 70–120 °C, and a heating rate of 3 °C/min for temperatures in the range of 120–150 °C. The measured temperature precision for  $T_h$  was  $\pm 1$  °C. The manufacturer's stated accuracy for the calibration standards (synthetic reference inclusions) is better than 1 °C over the range of temperatures reported here. The  $T_h$  were measured when all of the inclusions were homogenized in the liquid phase and the size of the vapor

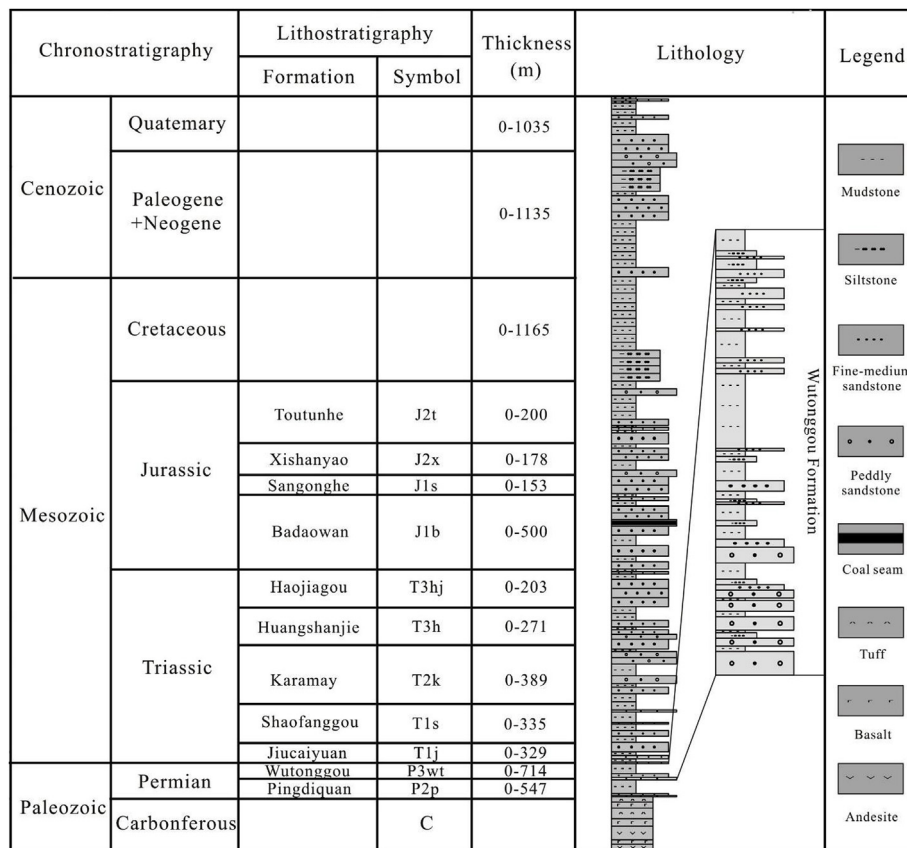


Fig. 2. Generalized stratigraphic column of the study area.

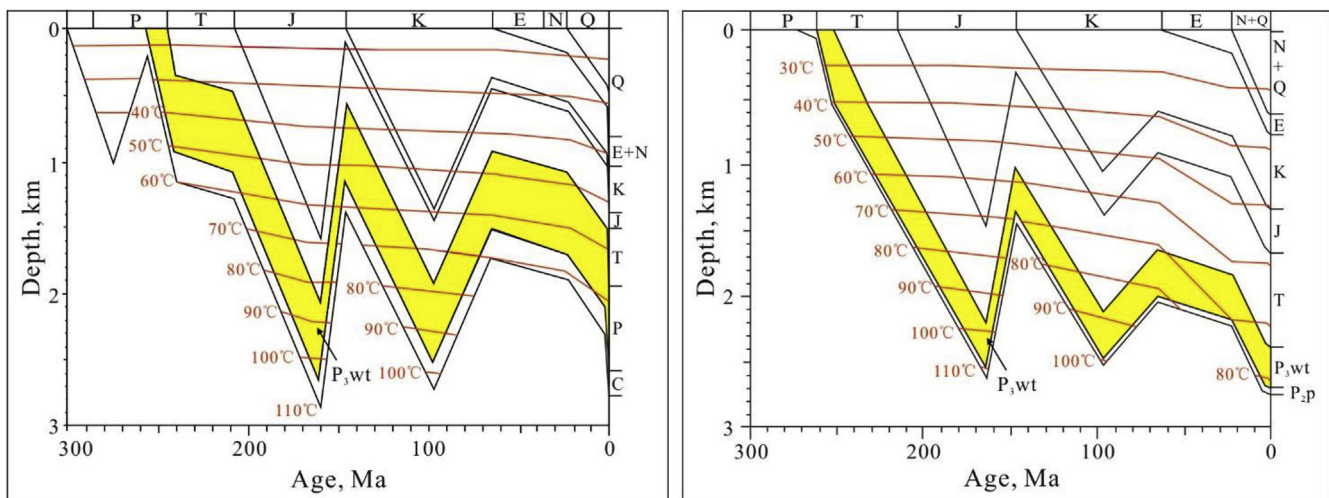
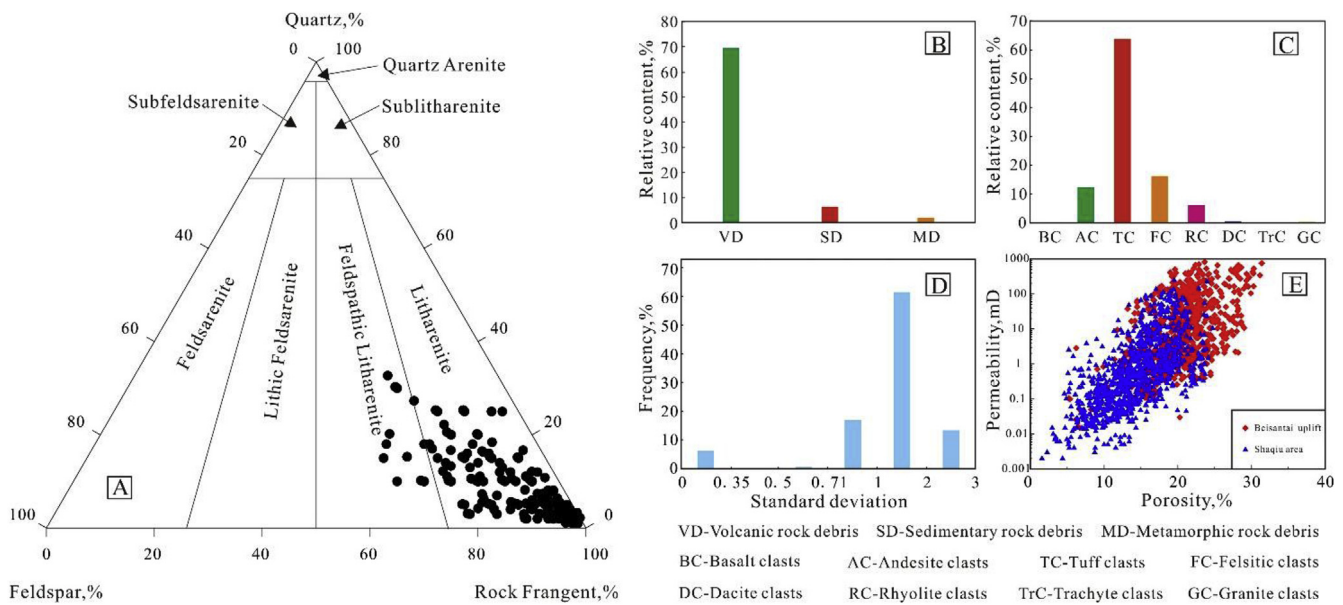


Fig. 3. Burial and thermal histories of Well B-16 (left) and Well Sha-107 (right) in the study area.

phase in these inclusions did not change after cooling to room temperature after the  $T_h$  measurements. The freezing-point temperatures (last melting temperatures) of the aqueous fluid inclusions were observed at heating rates of 5 °C/min after freezing at -80 °C. The salinities were calculated from the freezing-point temperatures using equations provided by Bodnar (1993) and were expressed as wt% NaCl equivalent. All of the inclusions in the calcites were from a fluid inclusion plane and some of the inclusions in the quartz were from the single inclusion plane but the other inclusions in the quartz were isolated. Micro-drilling of the four samples with different kinds of carbonate cements was conducted using a micro-drill system with a 100- $\mu$ m drill at the Institute of Geology and Geophysics at the Chinese Academy

of Sciences (IGGCAS) in Beijing. First, we observed the thin sections under CL and selected areas filled with pure calcite or ferroan calcite cements. Microphotographs were obtained of these areas and the thin sections were marked. Finally, the marked calcite or ferroan calcite cements were drilled using the micro-drill system. Subsequently, we divided every sample into two parts with a weight of 2 mg each. Eight samples were used for O and C stable isotope analysis, which was conducted using a MAT253 stable isotope mass spectrometer at the China University of Geosciences (Wuhan). The  $\delta^{13}C$  and  $\delta^{18}O$  values were determined by  $CO_2$  from the powdered carbonate samples dissolved by 100%  $H_3PO_4$  at 50 °C. The measured precision for  $^{13}C$  and  $^{18}O$  was less than 0.2‰. The isotopic composition of  $CO_2$  is reported in



**Fig. 4.** A: Ternary plot showing the rock composition and the rock type of the Permian reservoirs in the eastern slope of Fukang Sag (Folk, 1980). B: Histogram showing the relative contents of the volcanic, sedimentary, and metamorphic rock fragments in the eastern slope of Fukang Sag. C: Histogram showing the relative contents of different types of volcanic rock fragments. D: Histogram showing the standard deviations of the sandstones of the Wutonggou Formation in the study area. E: Scatterplot of porosity versus permeability in the Beisantai uplift and Shaqiu area.

units of ‰ relative to V-PDB. The EPMA was conducted using a JEOLJXA-8230 microanalyzer at the Ocean University of China; it had an acceleration voltage of 20 kV, an electric current of  $1 \times 10^{-8}$  A, and a spot size of 5–10  $\mu\text{m}$ . The chemical analyses by EPMA yielded values that were accurate to within about 1 wt% for the major elements and 3 wt% for the trace elements. The element analysis was calibrated using natural and synthetic standards and the following materials: SrO-celestite,  $\text{Na}_2\text{O}$ -albite, MgO-diopside,  $\text{SiO}_2$ -diopside,  $\text{K}_2\text{O}$ -sanidine, CaO-diopside,  $\text{TiO}_2$ -benitoite, FeO-hematite, MnO-bustamite, and  $\text{C}_2\text{O}_3$ -chromium oxide.

## 4. Results

### 4.1. Lithology

The sandstones of the Wutonggou Formation in the study area mainly consist of fine-medium sandstones and pebbly sandstones. The standard deviations of the particle size vary between 1 and 2, exhibiting relatively poor sorting (Fig. 4D). The detrital grains are mainly sub-angular to sub-rounded. The sandstones are dominated by litharenite and feldspathic litharenite based on the thin section analysis (Fig. 4A). The quartz proportion ranges from 2.1% to 19.5%, with an average of 9.7%. The feldspar content ranges from 1.4% to 18.2%, with an average of 9.9%. The debris content ranges from 70.2% to 89.8%, with an average of 79.8%. Volcanic lithic fragments dominate the detrital grains and are mainly composed of tuff clasts, andesite clasts, and felsite clasts (Fig. 4C). Some sedimentary debris and metamorphic debris are also observed (Fig. 4B). The cements include carbonate, laumontite, kaolinite, chlorite, illite, and authigenic quartz. The matrix content ranges from 0 to 1% with an average of 0.7%. The porosity ranges from 10.06% to 24.95% with an average of 17.2% and the permeability mainly ranges from 0.11 mD to 99.46 mD with an average of 31 mD in the Wutonggou Formation. In general, the reservoir quality is higher in the Beisantai uplift than in the Shaqiu area (Fig. 4E).

### 4.2. Authigenic minerals

Carbonates and laumontites are major authigenic minerals. They are relatively common in the study area. Furthermore, authigenic quartz

and clay minerals are developed as well in the study area.

#### 4.2.1. Carbonate

Based on the thin section observations, carbonate minerals are the most common authigenic minerals in the clastic reservoirs of the Permian Wutonggou Formation. Two types of carbonate cements were identified by the thin sections, CL, isotope tests, and electron probe analysis. One type is sparry calcite with red dyeing and orange-red luminescence. The other type is sparry ferroan calcite with purple dyeing and dark red luminescence (Fig. 5A, B, C, D). The calcite is characterized by filling the dissolution pores of laumontites (Fig. 5G), growing along the edges of the particles (Fig. 5E and F), and being dissolved partially (Fig. 5H).

The sparry ferroan calcite generally grows in the center of the pores (Fig. 5E). Unfortunately, sparry carbonates are characterized by complete crystal forms and perfect cleavages. These carbonate features indicate that they have difficulty capturing a large number of primary inclusions. In this study, we only found a limited number of two-phase aqueous fluid inclusions, mono-phase hydrocarbon inclusions with yellow fluorescence in calcites (Fig. 5I and J), and mono-phase hydrocarbon inclusions with blue fluorescence in the ferroan calcites (Fig. 5K and L). The homogenization temperature of the aqueous fluid inclusions in the calcites (Fig. 6) ranges from 118.5 to 135.2 °C (Table 1). The salinities of these inclusions range from 8.81 to 10.73 wt % (Table 1). The morphologies of the inclusions in the calcites are mostly oval or polygonal and do not show any obvious signs of stretching or partial leakage (Fig. 6A). On this basis, we collected samples of two types of carbonate cements from thin sections carefully by micro-drilling and measured their O and C stable isotope ratios (Table 2).

The results show that the calcites contain negative values of  $\delta^{13}\text{C}$  and  $\delta^{18}\text{O}$ , ranging from  $-18.42\text{‰}$  to  $-19.40\text{‰}$  for the  $\delta^{13}\text{C}_{(\text{V-PDB})}$  values and  $-17.2\text{‰}$  to  $-18.08\text{‰}$  for the  $\delta^{18}\text{O}_{(\text{V-PDB})}$  values. In contrast, the characteristics are similar for the oxygen isotopes but quite different for the carbon isotopes. One kind is characterized by the values of  $-5.94\text{‰}$  and  $-6.00\text{‰}$  for  $\delta^{13}\text{C}_{(\text{V-PDB})}$  and  $-15.59\text{‰}$  and  $-15.85\text{‰}$  for  $\delta^{18}\text{O}_{(\text{V-PDB})}$ . The other kind is characterized by the values of  $+22.10\text{‰}$  and  $+22.16\text{‰}$  for  $\delta^{13}\text{C}_{(\text{V-PDB})}$  and  $-15.27\text{‰}$  and  $-15.49\text{‰}$  for  $\delta^{18}\text{O}_{(\text{V-PDB})}$ .

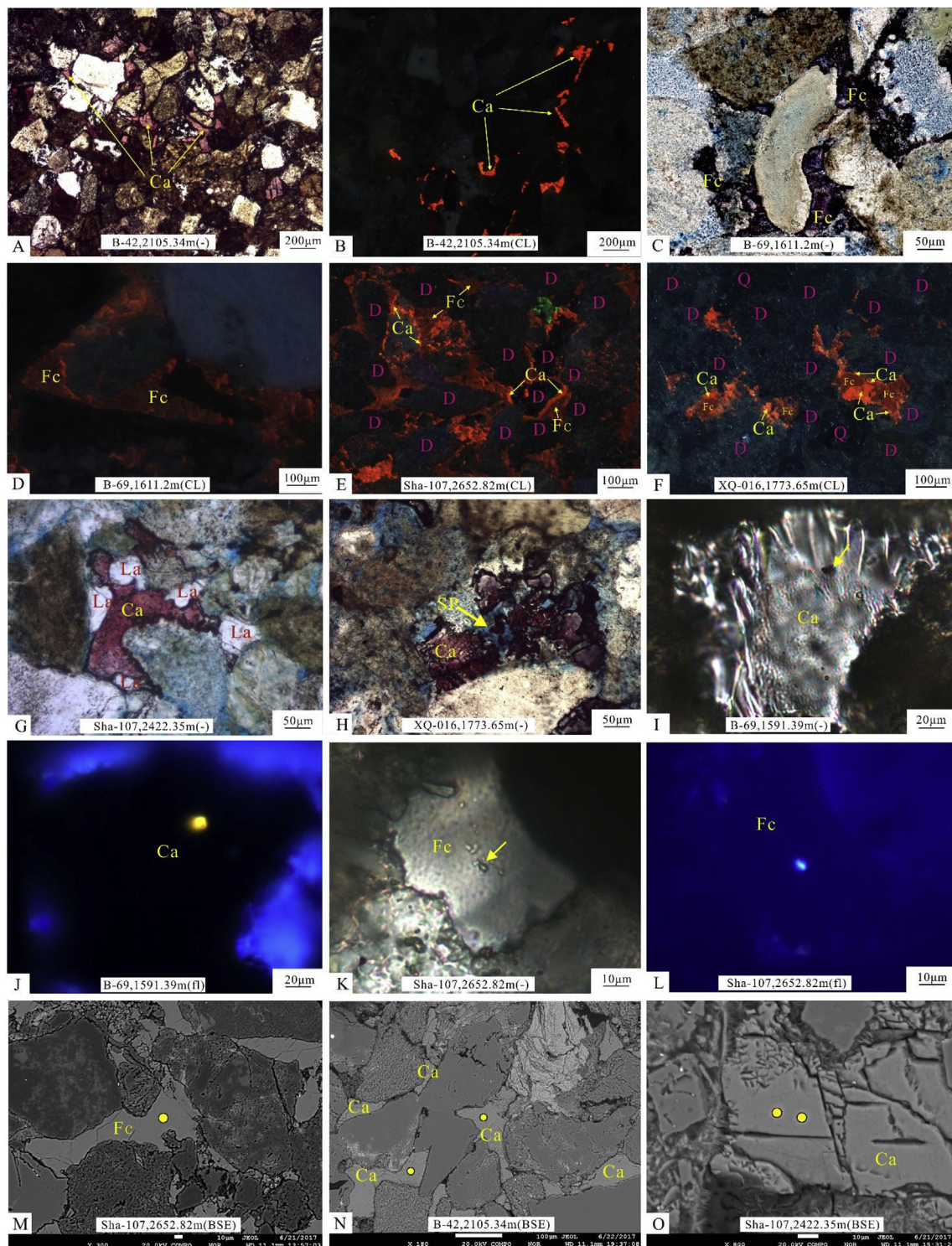


**Fig. 5.** Petrographic images of sparry carbonate in the Permian sandstones. A: Calcites in dyed cast thin section. B: Characteristics of calcites under CL. C: Ferroan calcites in dyed cast thin sections. D: Characteristics of ferroan calcites under CL. E-F: Characteristics of calcites and ferroan calcites under CL, calcites developed along the particle boundaries and ferroan calcites developed in the center of pores. G: Secondary pores of laumontites filled by sparry calcites. H: Dissolution characteristics of calcites I: Hydrocarbon inclusion trapped in the sparry calcite. J: Hydrocarbon inclusion with yellow fluorescence. I and J show the same inclusion under polarized light and fluorescence and the images were captured in the same visual field. K: Hydrocarbon inclusion contained by the sparry ferroan calcite. L: Hydrocarbon inclusion with blue fluorescence. K and L show the same inclusion under polarized light and fluorescence and the images were captured in the same visual field. M: BSE image of ferroan calcites; N-O: BSE images of calcites. Ca-sparry calcites; Fc-sparry ferroan calcites; K-authigenic kaolinite; Fl-fluorescence; SP-secondary pores; the arrows indicate the locations of hydrocarbon inclusions; solid circles with yellow color show the areas analyzed by the microprobe. (For interpretation of the references to color in this figure legend, the reader is referred to the Web version of this article.)

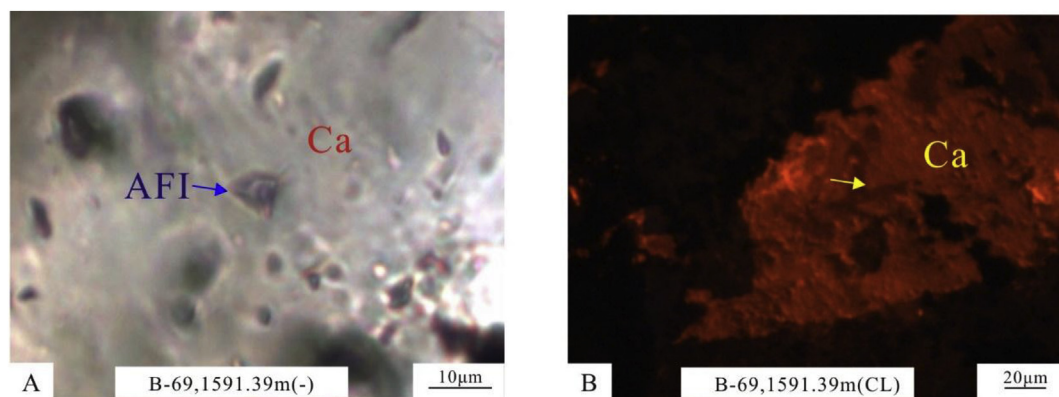


**Fig. 6.** Images of aqueous fluid inclusions (AFI) in calcite in the Permian sandstones. A: Inclusion contained in calcite. B: The characteristics of the calcite with the AFI in picture A under CL; Ca-calcite.

**Table 1**

Microthermometric data of AFI in the Permian sandstones on the eastern slope of the Fukang Sag. Ca: sparry calcites; Qo: Quartz overgrowth; Qmf: healed microfracture in quartz;  $T_h$ : homogenization temperature.

Well	Depth, m	Host minerals	Size, $\mu\text{m}$	$T_h$ , $^{\circ}\text{C}$	Freezing point, $^{\circ}\text{C}$	Salinity, wt % NaCl eq
B-69	1591.39	Ca	3.4	132.7	-6.7	10.11
B-69	1591.39	Ca	4.8	126.1		
B-69	1591.39	Ca	5.1	119.9	-6.3	9.60
B-69	1591.39	Ca	7.6	123.3	-6.3	9.60
B-69	1591.39	Ca	2.2	128.4	-6.8	10.24
B-69	1591.39	Ca	2.3	124.5	-5.7	8.81
B-69	1591.39	Ca	3.1	130.5	-7.2	10.73
B-16	2114	Qmf	6.1	129.6	-6.9	10.36
B-16	2114	Qmf	3.1	130.2	-6.9	10.36
B-16	2283.55	Qo	3.3	121.7	-5.7	8.81
B-16	2319.06	Qo	6.1	137.05	-7.2	10.79
B-16	2319.4	Qo	2.7	105.7	-5.1	8.00
Sha-107	2422.35	Qo	2.1	81.8	-4.5	7.17
Sha-107	2422.35	Qo	3.3	85	-4.5	7.17
Sha-107	2422.35	Qo	3.2	112.9	-5.8	8.96
Sha-107	2422.35	Qo	3.5	123.4	-8.4	12.16
Sha-107	2422.35	Qmf	2.5	119.5	-5.5	8.55
Sha-107	2422.35	Qmf	5.1	112.1	-5.5	8.55
Sha-107	2422.35	Qmf	4.8	115.2	-5.7	8.81
Sha-107	2652.82	Qo	3.1	135.1	-6.7	10.1

**Table 2**

Isotopic composition of carbonate cements in the Permian sandstones. Ca: sparry calcites; Fc: sparry ferrocalcite.

Well	Depth, m	Carbonate cements	$\delta^{13}\text{C}_{\text{V-PDB}}$ , ‰	$\delta^{18}\text{O}_{\text{V-PDB}}$ , ‰
B-69	1591.39-A	Ca	-19.40	-17.2
B-69	1591.39-B	Ca	-18.52	-17.45
B-69	1611.2-A	Fc	+22.16	-15.49
B-69	1611.2-B	Fc	+22.10	-15.27
Sha-107	2422.35-A	Ca	-18.42	-17.74
Sha-107	2422.35-B	Ca	-19.06	-18.08
Sha-107	2652.82-A	Fc	-6.00	-15.85
Sha-107	2652.82-B	Fc	-5.94	-15.59

In addition, we conducted the EPMA on the calcites and ferroan calcites (Table 3) (Fig. 5M–O). The results show that the calcites possess similar elemental characteristics. For example, the contents of Fe, Mn, Cr, and Mg are similar in the calcites from different locations (Fig. 7A–D). However, the ferroan calcites have more enrichment of Fe, Mn, Cr, and Mg than the calcites. Furthermore, compared to the ferroan calcites with a negative  $\delta^{13}\text{C}_{\text{(V-PDB)}}$ , the ferrocalcites with a positive  $\delta^{13}\text{C}_{\text{(V-PDB)}}$  are richer in Fe (Fig. 7A–D).

#### 4.2.2. Laumontite

Zeolite cements are important authigenic minerals in most sandstones with abundant volcanic lithic fragments (Noh and Lee, 1999). In the Permian sandstones, zeolite cements are dominated by laumontite. Laumontites occur as pore-filling cements and are characterized by well-developed cleavages. Some laumontites are dissolved (laumontite-I) and some are not (laumontite-II) (Fig. 8A–F). Hydrocarbon inclusions were not found in the partially dissolved laumontites (laumontites-I) and the dissolution pores in them were filled by authigenic kaolinite. Occasionally, the residual spaces in their dissolution pores are filled by hydrocarbon with yellow fluorescence, except for the spaces filled by authigenic kaolinite (Fig. 8A, B, G, H).

The hardly dissolved laumontites (laumontites-II) are characterized by containing hydrocarbon inclusions with yellow or blue fluorescence (Fig. 8I–L). The rock debris or feldspars with the dissolution pores are partly surrounded by laumontites-II (Fig. 8C–D). Simultaneously, the laumontites-I and the laumontites-II can occur in the same thin section, even in the same intergranular pore (Fig. 8E and F). Focusing on the laumontites-I and the laumontites-II with the yellow or blue fluorescent hydrocarbon inclusions, we conducted EPMA on the selected samples (Table 3) (Fig. 8G–O). The results show the obvious differences in these two types of laumontites (Fig. 7E–J). The laumontites-I are characterized by a higher CaO/Na<sub>2</sub>O ratio and a lower Fe content than the laumontites-II (Fig. 7F, I, J); the contents of Fe, Mn, Cr, and Mg are higher in the laumontites-II with the blue fluorescent hydrocarbon inclusions than in the laumontites-I with the yellow fluorescent hydrocarbon inclusions (Fig. 7E–H).

#### 4.2.3. Authigenic quartz

The content of authigenic quartz is relatively low in the Wutonggou Formation. The authigenic quartz is mainly characterized by quartz overgrowth and the content ranges from 0.5 to 2% with an average of 0.525% (Fig. 9A and B). Quartz overgrowths are also observed to be engulfed by calcites (Fig. 9C and D). The microthermometry results of the inclusions in the authigenic quartz showed that they were formed in the range of 81.8–137.5  $^{\circ}\text{C}$  and the freezing-point temperature ranged from -4.5 to -8.4  $^{\circ}\text{C}$  with a salinity from 7.17 to 12.16 wt% (Table 1). The morphologies of the inclusions in the authigenic quartz are mostly oval. According to the burial history curve, some of the authigenic quartz was formed at temperatures higher than the normal burial temperature (Fig. 3). The hydrocarbon inclusions also developed in the quartz overgrowths (Fig. 9E and F). The EPMA analyses indicated that the quartz overgrowths contained the elements of Al, Ca, and Fe in addition to the quartz particles (Table 3).

#### 4.2.4. Clay minerals

The clay minerals in the study area mainly include kaolinite, chlorite, and illite. Kaolinite is present in a vermicular form and as

**Table 3**  
 EPMA results for different types of cements (carbonate, laumontite, and quartz overgrowth) in the Permian sandstones. Ca: sparry calcites with yellow fluorescent hydrocarbon inclusions; Fc: sparry ferroan calcites with blue fluorescent hydrocarbon inclusions; La-I: laumontites with dissolution pores; the secondary pores formed by dissolution were filled by authigenic kaolinite and hydrocarbon; La-II: hardly dissolved laumontites with yellow fluorescent hydrocarbon inclusions; La-III: hardly dissolved laumontites with blue fluorescent hydrocarbon inclusions; Q: quartz grains; Qo-I: quartz overgrowths from different quartz particles; ULOD: under limit of detection.

Number	Well	Depth,m	Cement type	SrO, %	MgO, %	SiO <sub>2</sub> , %	K <sub>2</sub> O, %	CaO, %	TiO <sub>2</sub> , %	FeO, %	MnO, %	Cr <sub>2</sub> O <sub>3</sub> , %	Al <sub>2</sub> O <sub>3</sub> , %	Na <sub>2</sub> O, %
1	B-69	1591.39	Ca	0(ULOD)	0.035	0.284	0(ULOD)	53.5	0(ULOD)	0.078	0.851	0.005(ULOD)	/	/
2	B-69	1591.39	Ca	0.042	0.02	0.398	0.084	55.832	0.012(ULOD)	0.056	0.312	0(ULOD)	/	/
3	B-69	1591.39	Ca	0(ULOD)	0.061	0.765	0.09	53.7	0.038	0.105	0.839	0.024	/	/
4	Sha-107	2422.35	Ca	0(ULOD)	0.021	0(ULOD)	0.002(ULOD)	55.526	0(ULOD)	0.075	1.044	0(ULOD)	/	/
5	Sha-107	2422.35	Ca	0(ULOD)	0.005(ULOD)	0(ULOD)	0.002(ULOD)	55.055	0(ULOD)	0.04	0.928	0(ULOD)	/	/
6	Sha-107	2422.35	Ca	0.039	0.003(ULOD)	0(ULOD)	0(ULOD)	55.006	0.018(ULOD)	0.055	1.026	0.011(ULOD)	/	/
7	Sha-107	2422.35	Ca	0.041	0.009(ULOD)	0.032	0.009(ULOD)	55.373	0(ULOD)	0.115	0.745	0.002(ULOD)	/	/
8	Sha-107	2422.35	Ca	0.051	0.037	0.024	0.013	56.652	0(ULOD)	0.055	0.718	0(ULOD)	/	/
9	B-42	2105.34	Ca	0(ULOD)	0.005(ULOD)	0.025	0(ULOD)	54.815	0(ULOD)	0.09	0.361	0(ULOD)	/	/
10	B-42	2105.34	Ca	0(ULOD)	0.012(ULOD)	0.032	0.007(ULOD)	54.342	0.015(ULOD)	0.09	0.642	0(ULOD)	/	/
11	B-42	2105.34	Ca	0(ULOD)	0.016	0.025	0.003(ULOD)	54.683	0.024	0.024	0.469	0.013(ULOD)	/	/
12	B-42	2105.34	Ca	0(ULOD)	0.027	0.031	0(ULOD)	54.478	0(ULOD)	0.03	0.566	0.008(ULOD)	/	/
13	B-42	2105.34	Ca	0(ULOD)	0.01(ULOD)	0.124	0.013	57.058	0(ULOD)	0.157	0.384	0.01(ULOD)	/	/
14	B-16	2284.73	Ca	0.017	0(ULOD)	0.027	0(ULOD)	57.949	0(ULOD)	0.135	1.116	0.043	/	/
15	B-69	1611.2	Fc	0.051	0.068	0.105	0.041	51.373	0(ULOD)	1.44	1.482	0(ULOD)	/	/
16	B-69	1611.2	Fc	0.027	0.069	0.066	0.012(ULOD)	52.919	0.008(ULOD)	1.209	1.408	0.03	/	/
17	B-69	1611.2	Fc	0(ULOD)	0.03	0(ULOD)	0.016	51.78	0(ULOD)	1.496	1.689	0.046	/	/
18	Sha-107	2652.82	Fc	0.048	0.191	0.008(ULOD)	0(ULOD)	52.258	0(ULOD)	0.873	4.05	0(ULOD)	/	/
19	Sha-107	2652.82	Fc	0.033	0.238	0.032	0(ULOD)	52.913	0.004(ULOD)	0.9	3.116	0.051	/	/
20	Sha-107	2652.82	Fc	0(ULOD)	0.261	0.018(ULOD)	0.015	53.11	0(ULOD)	0.966	3.045	0.013(ULOD)	/	/
21	Sha-107	2652.82	Fc	0.071	0.212	0.092	0.037	53.942	0(ULOD)	1.057	3.782	0.021	/	/
22	B-42	2087.4	La-I	0.286	0.007(ULOD)	52.253	0.223	10.94	0(ULOD)	0.027	0.008(ULOD)	0.006(ULOD)	20.377	0.177
23	B-42	2087.4	La-I	0.367	0.007(ULOD)	53.222	0.193	10.906	0(ULOD)	0.034	0.007(ULOD)	0.015(ULOD)	20.777	0.12
24	B-42	2087.4	La-I	0.345	0.009(ULOD)	53.266	0.164	11.101	0(ULOD)	0.063	0.028	0.035	20.987	0.063
25	B-42	2087.4	La-I	0.34	0(ULOD)	54.373	0.163	11.266	0.002(ULOD)	0.066	0.018	0.003(ULOD)	21.163	0.114
26	B-42	2087.4	La-I	0.353	0.011(ULOD)	55.076	0.198	11.072	0.013(ULOD)	0.028	0.004(ULOD)	0(ULOD)	21.177	0.13
27	B-42	2087.4	La-I	0.384	0(ULOD)	52.948	0.179	10.864	0(ULOD)	0.043	0(ULOD)	0(ULOD)	20.123	0.126
28	B-42	2087.4	La-I	0.301	0.017	53.337	0.214	11.045	0(ULOD)	0.065	0(ULOD)	0.023	20.499	0.049
29	B-42	2087.4	La-I	0.288	0.011(ULOD)	54.854	0.183	10.833	0(ULOD)	0.06	0(ULOD)	0(ULOD)	21.422	0.083
30	B-42	2087.4	La-I	0.306	0(ULOD)	52.989	0.2	11.249	0(ULOD)	0.01(ULOD)	0.011(ULOD)	0(ULOD)	20.6385	0.018
31	Sha-107	2422.35	La-I	0.266	0.006(ULOD)	52.574	0.14	10.669	0.006(ULOD)	0.059	0(ULOD)	0.047	20.427	0.073
32	B-42	2087.4	La-II	0.301	0.016	53.774	0.26	10.48	0(ULOD)	0.046	0(ULOD)	0(ULOD)	20.281	0.379
33	B-42	2087.4	La-II	0.258	0(ULOD)	53.693	0.186	10.604	0(ULOD)	0.044	0.011(ULOD)	0.012(ULOD)	20.614	0.559
34	B-42	2087.4	La-II	0.396	0(ULOD)	53.131	0.177	10.891	0(ULOD)	0.04	0(ULOD)	0(ULOD)	20.56	0.197
35	B-42	2087.4	La-II	0.365	0.01(ULOD)	52.622	0.203	10.662	0.008(ULOD)	0.045	0(ULOD)	0(ULOD)	20.367	0.227
36	B-42	2087.4	La-II	0.236	0(ULOD)	54.395	0.257	10.631	0.061	0.11	0(ULOD)	0(ULOD)	20.435	0.203
37	B-42	2087.4	La-II	0.275	0.012(ULOD)	53.975	0.177	10.683	0(ULOD)	0.127	0.001(ULOD)	0.006(ULOD)	20.678	0.225
38	B-42	2087.4	La-II	0.282	0.005(ULOD)	53.348	0.22	10.776	0(ULOD)	0.131	0(ULOD)	0(ULOD)	20.444	0.426
39	B-42	2087.4	La-II	0.28	0.005(ULOD)	53.495	0.193	10.73	0.005(ULOD)	0.117	0.008(ULOD)	0.029	20.948	0.308
40	Sha-107	2422.35	La-II	0.339	0.014	53.064	0.114	10.733	0(ULOD)	0.082	0(ULOD)	0(ULOD)	20.432	0.362
41	SQ-2	2196.23	La-III	0.382	0.012(ULOD)	53.481	0.183	10.681	0(ULOD)	0.215	0.013(ULOD)	0.037	20.766	0.489
42	SQ-2	2196.23	La-III	0.365	0.021	53.069	0.136	10.665	0(ULOD)	0.136	0.035	0(ULOD)	20.437	0.403
43	SQ-2	2196.23	La-III	0.373	0(ULOD)	55.034	0.111	10.643	0(ULOD)	0.185	0.019	0.03	21.035	0.148
44	SQ-2	2196.23	La-III	0.306	0.015	54.026	0.133	10.967	0(ULOD)	0.193	0.042	0.024	20.828	0.469
45	SQ-2	2196.23	La-III	0.337	0.036	54.13	0.114	10.736	0(ULOD)	0.212	0.019	0.018	21.143	0.136
46	B-42	2087.4	Q	0.559	0(ULOD)	98.007	0(ULOD)	0.018	0(ULOD)	0(ULOD)	0.004(ULOD)	0.018	0.027	0(ULOD)
47	B-42	2087.4	Q	0.53	0.01(ULOD)	98.331	0.007(ULOD)	0.047	0.005(ULOD)	0.028	0(ULOD)	0.031	0.018	0.012(ULOD)
48	B-42	2087.4	Qo-I	0.495	0.003(ULOD)	100.547	0.004(ULOD)	0.073	0.039	0.014(ULOD)	0.023	0(ULOD)	0.226	0.022
49	B-42	2087.4	Qo-I	0.493	0(ULOD)	99.6	0.008(ULOD)	0.079	0(ULOD)	0.019	0(ULOD)	0(ULOD)	0.388	0.01(ULOD)
50	B-42	2087.4	Qo-I	0.504	0.003(ULOD)	100.069	0.003(ULOD)	0.073	0.031(ULOD)	0.037	0.01(ULOD)	0.024	0.624	0.032
51	B-42	2087.4	Qo-I	0.499	0(ULOD)	97.022	0.002(ULOD)	0.082	0(ULOD)	0.013(ULOD)	0(ULOD)	0.006(ULOD)	0.078	0.024

(continued on next page)

Table 3 (continued)

Number	Well	Depth,m	Cement type	SrO <sub>2</sub> , %	MgO <sub>2</sub> , %	SiO <sub>2</sub> , %	K <sub>2</sub> O, %	CaO, %	TiO <sub>2</sub> , %	FeO <sub>2</sub> , %	MnO <sub>2</sub> , %	Cr <sub>2</sub> O <sub>3</sub> , %	Al <sub>2</sub> O <sub>3</sub> , %	Na <sub>2</sub> O, %
52	B-42	2087.4	Qo-II	0.537	0.012(ULOD)	97.225	0.002(ULOD)	0.025	0(ULOD)	0.119	0.019	0.016	0.291	0.012(ULOD)
53	B-42	2087.4	Qo-II	0.492	0(ULOD)	97.144	0.006(ULOD)	0.031	0(ULOD)	0.079	0.002(ULOD)	0.004(ULOD)	0.213	0.006(ULOD)
54	B-42	2087.4	Qo-II	0.532	0(ULOD)	95.965	0.003(ULOD)	0.038	0(ULOD)	0.118	0(ULOD)	0.018	0.16	0(ULOD)

book-like stacked crystals. It is the most common clay mineral in the Permian sandstones (Fig. 10A). The authigenic kaolinites generally fill the intergranular pores and slightly fill the intragranular pores of the detrital feldspars (Fig. 9K and L). In the Shaqiu area, the authigenic kaolinite content is relatively high and ranges from 1.3% to 6.7% with an average of 3.66%. However, the contents of the authigenic kaolinite are clearly lower in the Beisantai uplift than in the Shaqiu area, ranging from 0.12% to 3% with an average of 1.56%. Chlorite occurs predominantly as grain coatings in the Permian sandstones and the coatings are generally perpendicular to the grain surfaces. The chlorite crystals are characterized by euhedral foliaceous morphology and cling tightly to the grain surfaces as is evident in the SEM observation (Fig. 10B). Illite occurs mainly as a fibrous and pore-bridging texture (Fig. 10C and D), which is identified at the depth ranges from 1630.54 m (5349.54 ft) to 2617.18 m (8586.55 ft). The kaolinites are occasionally replaced by fibrous illites in the Permian sandstones (Fig. 10E). Previous studies have suggested that the euhedral fibrous illites were the production of a late diagenesis (Wilkinson et al., 2014). In addition, the illitization of the kaolinite occurred from 120 to 140 °C in simulations and in present-day formations (Bjørlykke et al., 1989, 1995; Ehrenberg and Nadeau, 1989; Lander and Bonnell, 2010). These characteristics of illite indicate that the Permian sandstones have undergone relatively high temperatures.

## 5. Discussion

### 5.1. Genesis of carbonates

The feldspar contents and the carbonate rock debris are very low in the study area (Fig. 4A, C) and there is no obvious correlation between the carbonate contents and the distance from the mudstones adjacent to the sandstones cemented by the carbonate minerals (Fig. 11A). Based on these observations and the abundant volcanic lithic fragments (Fig. 4B), Ca would be mainly provided by the hydration of volcanic materials (Zhu et al., 2016). The tuff debris content has a good positive correlation with the calcite cement content when the tuff debris is less than 45% (Fig. 11B). However, owing to the relatively high plasticity of the tuff debris, the compaction gradually increases with increasing tuff debris content. The optical observations of the thin sections indicate that, at a similar burial depth, the particles exhibit a great abundance of point-to-point contact when the tuff debris content is less than 45%. In contrast, line and sutured grain contacts occur when the tuff debris content is greater than 45%. The increase of the tuff debris content gradually retains the diminishing residual pores, which cannot provide sufficient spaces for the abundant carbonate cementation (Fig. 11B).

Previous studies have indicated that the Permian sandstones underwent hydrocarbon charging during the Jurassic period (Wang, 1992; Liu et al., 2000). An intense tectonic uplift during the Late Jurassic induced the biodegradation of crude oil in the Beisantai uplift (Lu et al., 2011).

The calcites are <sup>13</sup>C and <sup>18</sup>O depleted (Table 1) and contain hydrocarbon inclusions with yellow fluorescence (Fig. 5I and J). The calcites appear to be dissolved in some areas and were impacted by meteoric water leaching (Fig. 5H). The characteristics of the meteoric water leaching will be discussed below. In addition, the  $\delta^{13}\text{C}_{\text{(V-PDB)}}$  values are not impacted by the CO<sub>2</sub> from the hydrocarbon biodegradation (Table 2) (Macaulay et al., 2000; Head et al., 2003; Zhu et al., 2008) and the elemental characteristics of the calcites are similar in the Beisantai and Shaqiu areas (Table 3). These results imply that the calcites developed after hydrocarbon charging and prior to the Late Jurassic. According to the tectonic evolution in the study area, a large-scale tectonic movement or orogeny would induce the external fluids (such as deep fluids) to flow into the reservoirs along the faults (Bjørlykke, 1993; Sadegh et al., 2008). The homogenization temperature of the aqueous fluid inclusions in the calcites indicates that the formation temperature of the calcites is higher than the burial temperatures

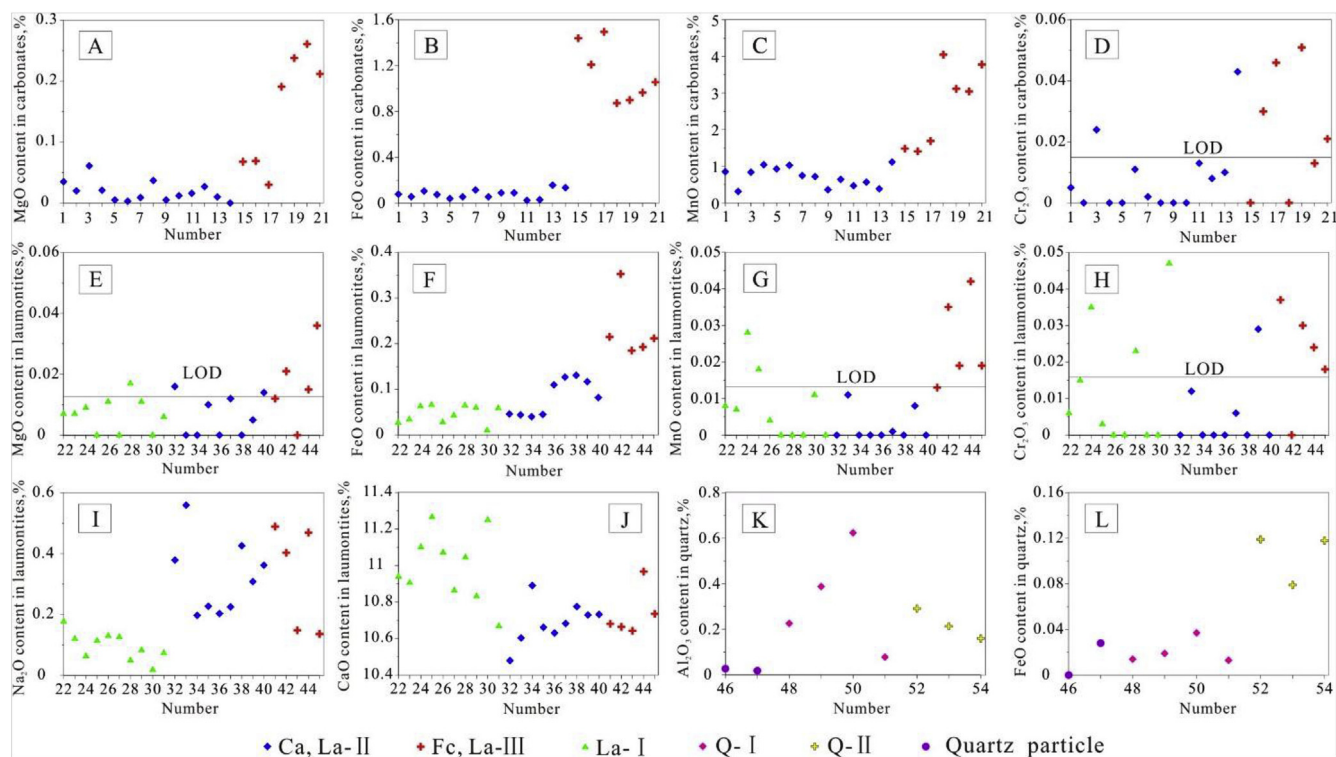


Fig. 7. Elemental composition based on EPMA in the carbonate cements, laumontite cements, and quartz overgrowth in the Permian sandstones. Ca-sparry calcites with yellow fluorescent hydrocarbon inclusions; Fc-ferroan calcites with blue fluorescent hydrocarbon inclusions; La-I-laumontites with dissolution pores and no hydrocarbon inclusions; La-II-hardly dissolved laumontites with yellow hydrocarbon inclusions; La-III-hardly dissolved laumontites with blue hydrocarbon inclusions; Q-I and Q-II-quartz overgrowths from different quartz particles; LOD-limit of detection. (For interpretation of the references to color in this figure legend, the reader is referred to the Web version of this article.)

(Table 1; Fig. 3). The fibrous-texture illites and the illitization of the kaolinites in the shallow strata also indicate that the Permian sandstones have undergone relatively high temperatures (Fig. 10C, D, E). Furthermore, the secondary pore content decreases with the increasing distance from the deep faults in the Shaqiu area (Fig. 12A) where the Permian sandstones are not impacted by meteoric water leaching (Table 4). The distribution of the carbonate cements exhibits similar characteristics (Fig. 12C). The formation temperatures of the calcites are higher than 119.9 °C, which indicates the occurrence of decarboxylation of organic matter or organic acid in the oil source fluid (Surdam and Crossey, 1985). The  $\delta^{13}\text{C}_{\text{(V-PDB)}}$  values ranged from  $-10\%$  to  $-25\%$ , which indicates that the origins of the carbon are mainly related to the decarboxylation of organic matter (Irwin et al., 1977). In addition, the isotopes with  $^{13}\text{C}$  and  $^{18}\text{O}$  depleted values were believed that the formation of calcites were mainly contributed by organic matter and deep fluids in Junggar Basin (Cao et al., 2007). These results confirmed that, together with the hydrocarbon migration, the deep fluids with the  $\text{CO}_2$  from the decarboxylation of organic matters flowed into the Permian sandstones during the middle-late Jurassic. The reservoirs adjacent to the deep faults were reconstructed by these external fluids that provided the carbon sources for the calcite formation (Duan et al., 2017).

The relationship between the calcites and ferroan calcites in the thin sections shows that the ferroan calcites developed relatively late (Fig. 5E). The distribution of the ferroan calcites is likely related to the distance from the deep faults (Fig. 12C). Unfortunately, we cannot find two-phase aqueous fluid inclusions but the  $\delta^{18}\text{O}_{\text{(V-PDB)}}$  values of the ferroan calcites were O-depleted (Table 2). However, especially in sandstones with abundant volcanic lithic fragments, changes in the temperature, the injection of external fluids, and water-rock reactions result in distinct changes in the  $\delta^{18}\text{O}_{\text{(V-PDB)}}$  values of the pore water (Noh and Lee, 1999; Marchand et al., 2002). During multi-stage

tectonic movements in the study area, a lot of volcanic material was hydrated and multiple diagenetic fluids were injected into the Permian sandstones, such as deep fluids, hydrocarbon, and meteoric water. These processes would result in multiple changes in the  $\delta^{18}\text{O}_{\text{(V-PDB)}}$  values of the pore water. Therefore, the formation temperature of the ferroan calcites calculated by using the equation from Friedman and O'Neil (1977) would be undefined in this context.

The  $\delta^{18}\text{O}_{\text{(V-PDB)}}$  values in the ferroan calcites are similar (Table 2); however, the  $\delta^{13}\text{C}_{\text{(V-PDB)}}$  values can be classified into two categories. One kind is characterized by the values of  $-5.94\%$  and  $-6.00\%$ , which shows that these ferroan calcites would be sourced by the mixed  $\text{CO}_2$  of both organic origin and inorganic origin (Bath et al., 1987; Hoefs, 2009; Xi et al., 2016). The other kind is characterized by the values of  $+22.10\%$  to  $+22.16\%$ , which shows that these ferroan calcites were sourced by the  $\text{CO}_2$  from the biodegradation of crude oil. Due to carbon isotope fractionation, the carbon isotopic composition of methane associated with hydrocarbon biodegradation is greatly  $^{13}\text{C}$ -depleted while the  $\text{CO}_2$  associated with hydrocarbon biodegradation is often enriched in  $^{13}\text{C}$ . Therefore, the ferroan calcites related to the  $\text{CO}_2$  from crude oil biodegradation are enriched in  $\delta^{13}\text{C}$  during the processes of fractionation (Macaulay et al., 2000; Head et al., 2003; Zhu et al., 2008). On this basis, Lu et al. (2011) proposed that the crude oil in the Beisantai uplift was biodegraded during an intense tectonic uplift during the Late Jurassic. In the Permian sandstones, the density and viscosity of the crude oil from the Beisantai uplift exhibit increases (Fig. 13A and B). The adjacent wells (DQ-3 and B-69) (Fig. 1) with similar burial depths as the Permian sandstones are all located on the Beisantai uplift. The density and viscosity of the crude oil from these two wells also show an obvious increase (Fig. 13A and B). Simultaneously, the chromatographic analysis results of the crude oil in the Permian sandstones from well DQ-3 show that the n-alkanes with low carbon numbers are strongly depleted in the crude oils and the peaks

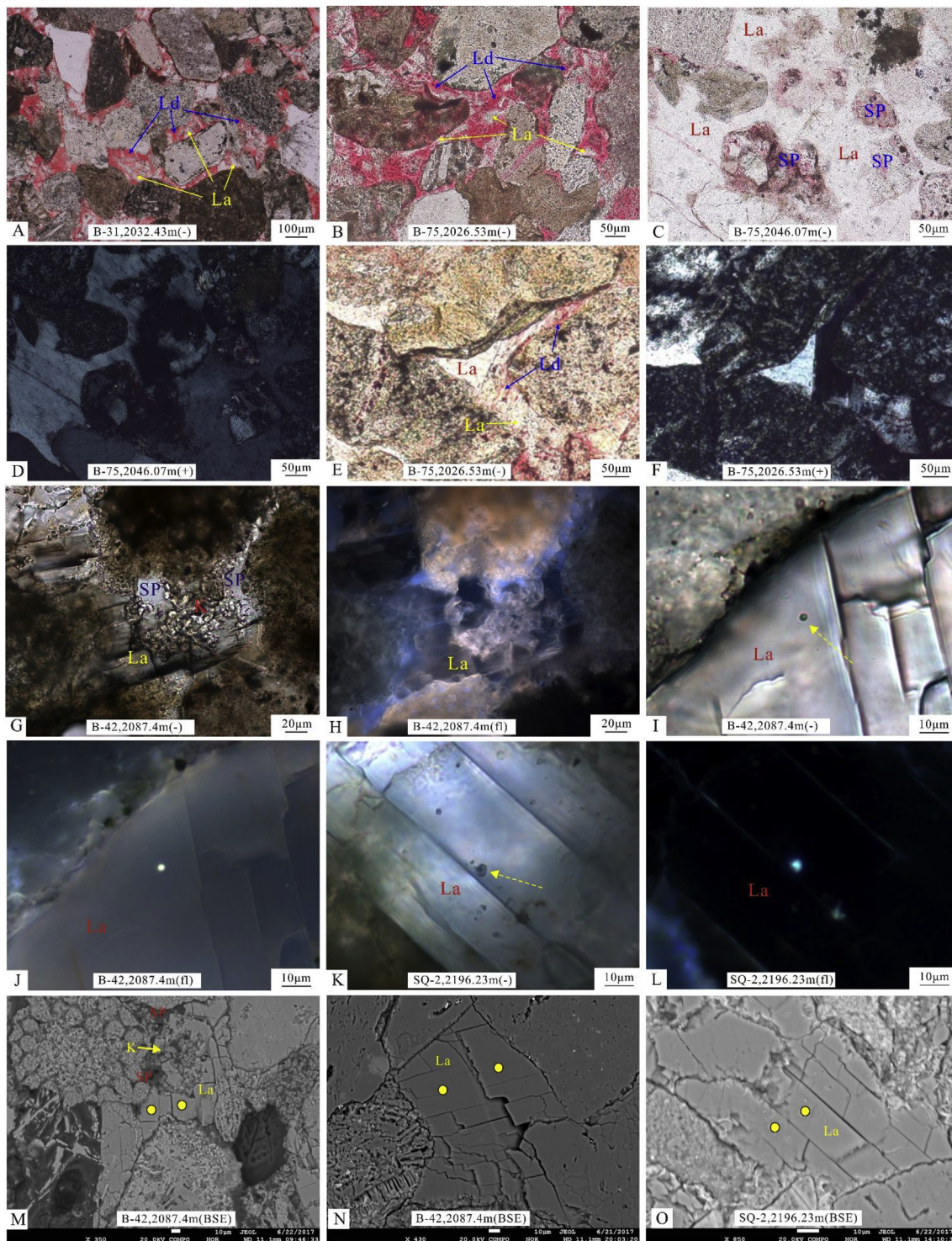


**Fig. 8.** Petrographic images of laumontite cements in the Permian sandstone (thin sections and BSE images). A-B: Intense dissolution of laumontite cements. C-D: The particles with the dissolution pores are surrounded by hardly dissolved laumontite cements; E-F: hardly dissolved laumontites and partially dissolved laumontites developed in the same intergranular pores. G-H: Secondary pores formed by the dissolution of laumontite filled by kaolinite and hydrocarbon with yellow fluorescence. I-J: hydrocarbon inclusion with yellow fluorescence contained by hardly dissolved laumontite cement. K-L: hydrocarbon inclusion with blue fluorescence contained by hardly dissolved laumontite cement. M: BSE image of the sample shown in G, H; N: BSE image of the sample shown in I, J; O: BSE image of the sample shown in K, L. La-laumontite cement; Ld-secondary pores formed by dissolution of laumontite cements; SP-secondary pores; K-authigenic kaolinite; the yellow dashed arrows indicate the locations of the hydrocarbon inclusions; solid circles with yellow color indicate the areas analyzed by the electron microprobe. (For interpretation of the references to color in this figure legend, the reader is referred to the Web version of this article.)

are superimposed on a very pronounced unresolved complex mixture (Fig. 13C). This indicates the characteristics of a biodegraded oil (Volkman et al., 1984; Head et al., 2003) and further demonstrates that

the formation of ferroan calcites enriched in  $\delta^{13}\text{C}$  from B-69 was impacted by the  $\text{CO}_2$  from the hydrocarbon biodegradation. These results also illustrate that the ferroan calcites were formed after the late

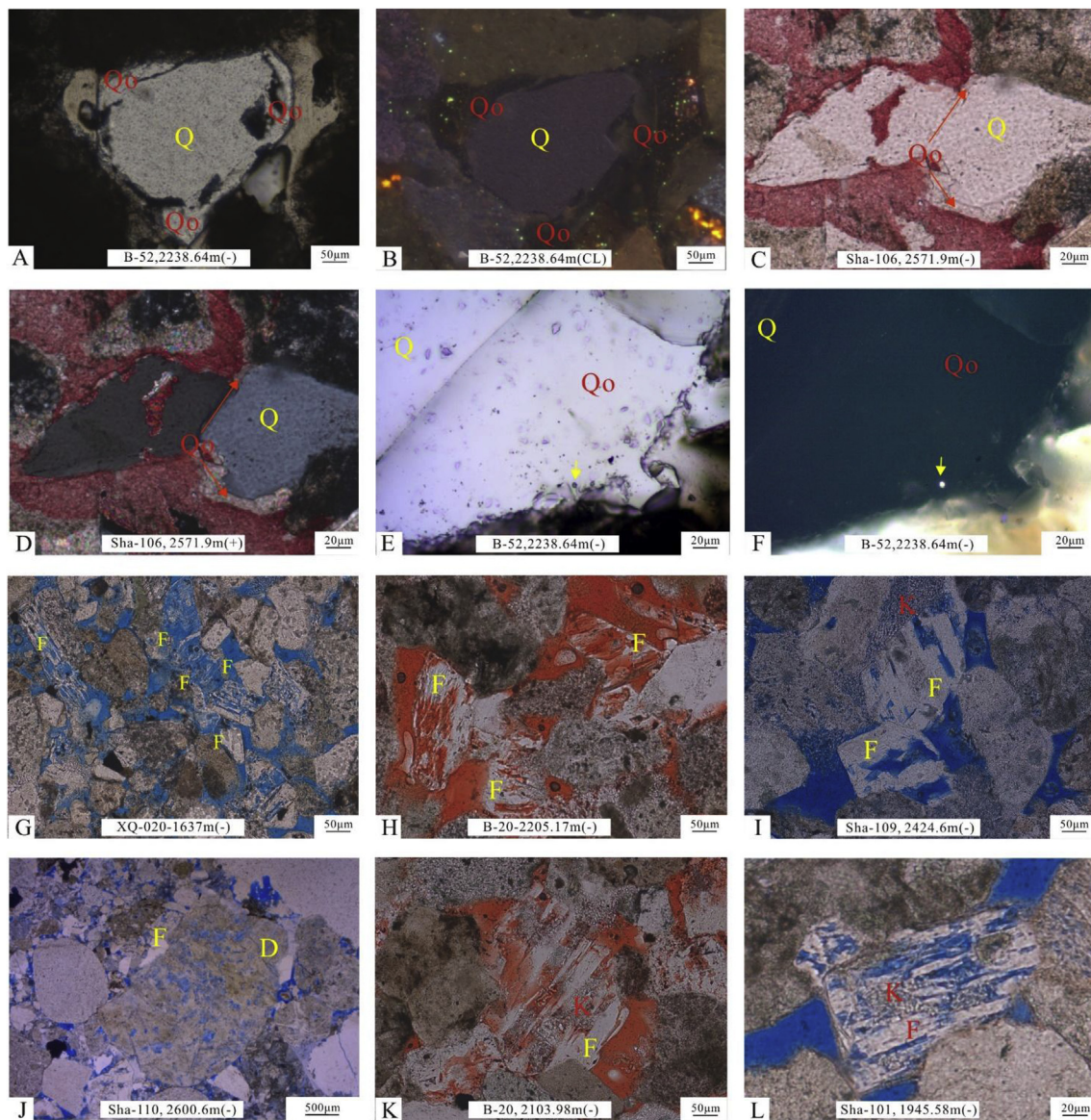


**Fig. 9.** Petrographic observations of the quartz overgrowths and dissolution characteristics in the Permian sandstones. A: detrital quartz and quartz overgrowths. B: characteristics of quartz overgrowth under CL. C-D: quartz overgrowth engulfed by calcite in the dyed cast thin section. E: hydrocarbon inclusions in quartz overgrowth. F: hydrocarbon inclusions in quartz overgrowth under fluorescence. E and F show the same inclusion under polarized light and fluorescence and the images were captured in the same visual field. G: intense dissolution of feldspars in the reservoir, which is 91 m in vertical distance to the unconformity. H-I: dissolution of feldspars in reservoirs. J: dissolution of debris in reservoirs. K-L: dissolution pores in feldspar filled by authigenic kaolinites. Q-quartz particles; Qo-quartz overgrowth; K-authigenic kaolinite; F-feldspar; D-debris.

#### Jurassic.

In addition,  $\text{Fe}^{3+}$  oxides would be sourced from the volcanic materials in the sandstones with abundant volcanic fragments (Sugitani et al., 2006), such as limonite and magnetite in the study area. During the biodegradation of hydrocarbon,  $\text{Fe}^{3+}$  oxides were reduced and the generated  $\text{Fe}^{2+}$  ions were released into the interstitial solutions (Irwin, 1980). The relative content of Fe in the interstitial solutions increased during this process and would cause the ferroan calcites in the Beisantai uplift to be richer in Fe than the ferroan calcites in the Shaqiu area (Fig. 7A–D). However, in general, sparry ferroan calcites contain relatively higher contents of Fe, Mn, Cr, and Mg than calcites. The differences in the fluorescence of the hydrocarbon inclusions, the isotope results, and the elemental characteristics also imply that the ferroan calcites developed from different diagenetic fluids.

#### 5.2. Genesis of laumontites

Based on the limited amount of plagioclases and the abundant volcanic materials in the Permian sandstones (Fig. 4A and B), the laumontites were most likely formed by volcanic material hydration during the burial stage (Fig. 11C). The hydration of volcanic materials can release abundant ions, such as  $\text{K}^+$ ,  $\text{Na}^+$ ,  $\text{Ca}^{2+}$ ,  $\text{Mg}^{2+}$ , and  $\text{Fe}^{2+}$ , which provide the source materials for the laumontite formations (Noh, 1998; Compton, 1999; Chipera et al., 2008; Zhu et al., 2012, 2016).

The analysis of the thin sections indicates that some laumontites are dissolved (laumontite-I) and some are not (laumontite-II), such as the samples in Well B-75 and B-42 (Fig. 8). The Wutonggou Formation in Well B-42 and B-75 developed in the fracture/fault systems in the Beisantai uplift and was impacted by meteoric water leaching during the Late Jurassic (Fig. 1C). The characteristics of meteoric water leaching will be discussed below. The intense dissolution of feldspars, debris, and laumontite cements can be observed in the thin sections

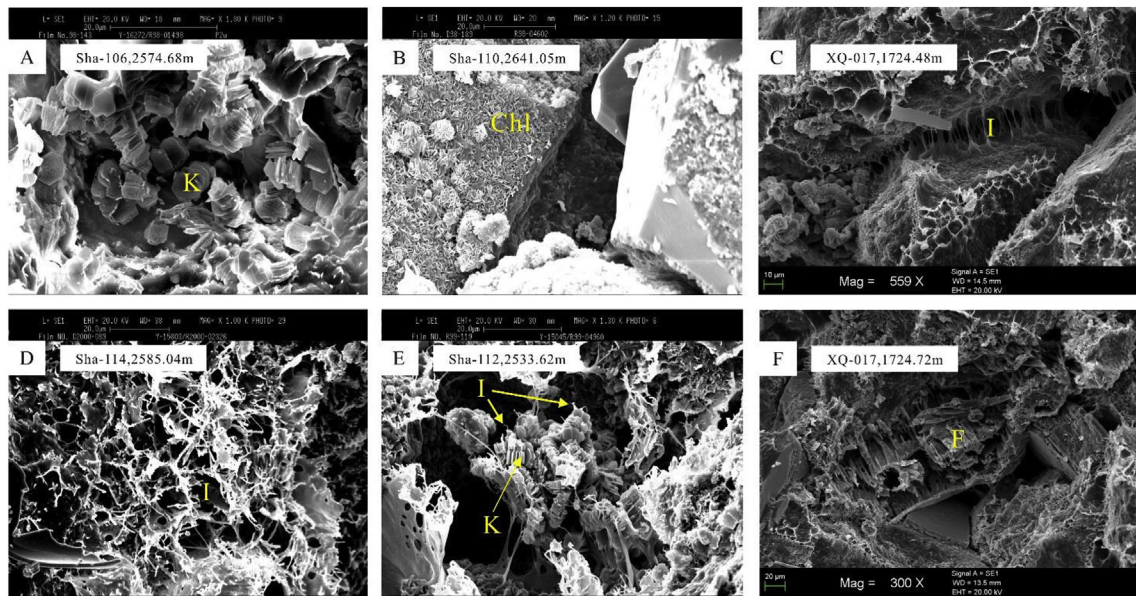


**Fig. 10.** SEM images of kaolinite, chlorite, illite, and feldspar dissolution in the Permian sandstones. A: authigenic kaolinites; B: chlorite coatings; C: illites with pore-bridging texture; D: illites with fibrous texture; E: illitization of authigenic kaolinites; F: intense dissolution of feldspar. K-authigenic kaolinite; Chl-chlorite; I-illite; F-feldspar.

(Fig. 8A, B, G, H). However, the rock debris or feldspars with the dissolution pores are partly surrounded by laumontites-II (Fig. 8 C, D). Furthermore, the laumontites-II are adjacent to the laumontite-I and these two types of laumontites can develop in the same pore (Fig. 8 E, F). Based on the differences in occurrences (Fig. 5G; 8A-F), the relationship between the hydrocarbon and laumontites (Fig. 8G–L), and the elemental characteristics (Fig. 7E–J), we tend to believe that these two types of laumontites are not contemporaneous cements. The secondary pores in the laumontites are filled by kaolinites, hydrocarbons, and calcites. This confirms that the laumontite-I were formed prior to hydrocarbon charging and calcite cementation. In contrast, the laumontites-II with the hydrocarbon inclusions indicate that they were formed after hydrocarbon charging and meteoric water leaching. The necessary ions provided for the laumontite formation are released by volcanic material hydration during the initial burial stage and the reburial stage (Noh, 1998). On these bases, the elemental characteristics in the minerals, such as laumontite and carbonate, mainly depend on the distribution of the elements in the mineral-forming solutions (Wopfner and Markwort, 1991; Drake et al., 2012). The relatively low Ca/Na ratios in the laumontites-II are likely related to the decrease in Ca due to precipitation of the carbonate cements (Gastmans et al., 2016). In comparison, the laumontites-I formed prior to the calcites are characterized by a relatively high Ca/Na ratios (Fig. 7I and J). Furthermore, the laumontites-I formed by the hydration of the volcanic

materials during the initial burial stage are characterized by a low Fe content, which implies that the additional Fe content in the laumontites-II depends on external supplements. The underlying Carboniferous strata and Permian formation includes abundant andesites, basalts, tuffs, and volcanic debris (Fig. 2). The hydration and alteration of these rocks releases Fe ions into the pore waters. As the deep fluid flows upward, the released Fe ions are moved into the Permian sandstones. This results in the increase in the Fe content in the laumontites-II (Fig. 7F). In addition, the laumontites-II with the blue fluorescent hydrocarbon inclusions show a relatively high content of Fe, Mn, Cr, and Mg compared to the laumontites-II with the yellow fluorescent hydrocarbon inclusions. The differences in the fluorescence characteristics of the hydrocarbon inclusions and in the elements imply that the laumontites-II likely developed from the different diagenetic fluids (Fig. 7E–H).

5.3. Genesis of authigenic quartz and clay minerals

The authigenic quartz, kaolinite, illite, and chlorite also developed in the Permian sandstones. The authigenic quartz overgrowths were replaced by calcite and contained hydrocarbon inclusions (Fig. 9C–F), which indicated that the authigenic quartz was formed during or after the oil emplacement but before the calcite cementations. The microthermometry of the inclusions in the authigenic quartz showed that

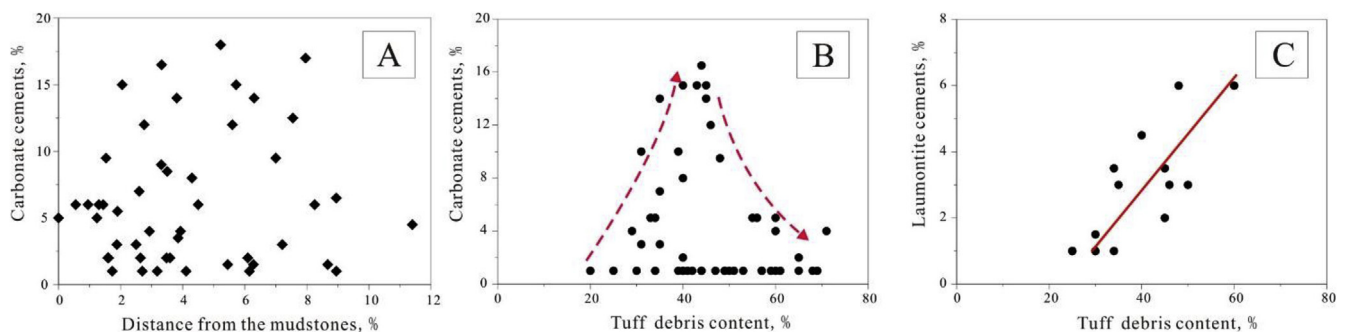


**Fig. 11.** A: Plot of distance from the mudstones versus the carbonate cement content. B: Plot of tuff debris content versus the carbonate cement content. C: Plot of tuff debris content versus the laumontite cement content. The content data was counted from the 2D thin sections.

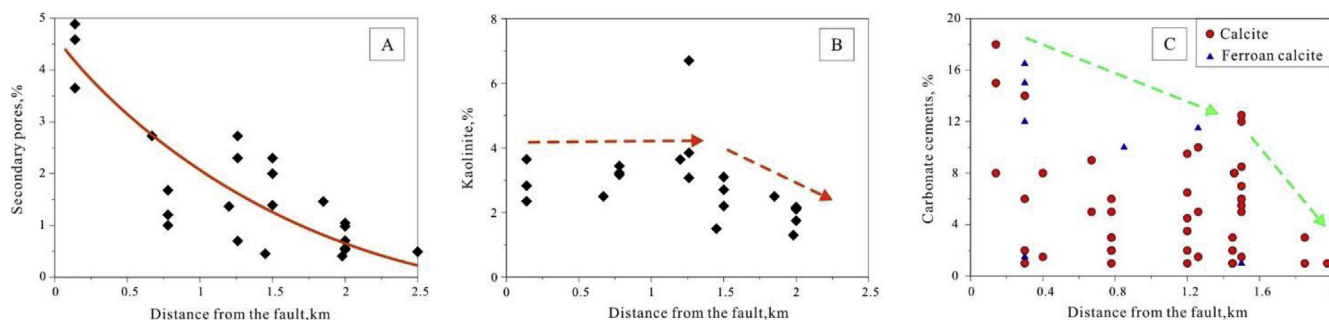


**Fig. 12.** Plots of distance from the fault versus the secondary pore content (A), the kaolinite content (B), and the carbonate cement content (C) in the Shaqiu area. The distance from the fault is the distance from the well to the nearest fault; the secondary pores include pores formed by the dissolution of feldspars, laumontites, and debris; the contents of the secondary pores, kaolinite, and the carbonate cements were enumerated from the thin sections.

**Table 4**

Trace elements of Permian mudstone interlayers in the eastern slope of the Fukang sag. “<DL>”: Below the detection limit.

Well	Cu,ppm	Cd,ppm	Zn,ppm	Cr,ppm	Ca,ppm	Ti,%	Mn,%
B-12	50	<DL>	100	100	<DL>	0.3	0.1
B-16	70	<DL>	40	100	<DL>	0.3	0.2
B-20	40	<DL>	70	92.5	<DL>	0.3	0.06
B-21	50	<DL>	50	100	<DL>	0.2	0.1
B-52	50	<DL>	40	70	<DL>	0.3	0.03
B-55	14.38	<DL>	28.75	88.75	<DL>	0.2	0.14
B-75	72.5	<DL>	25	60	<DL>	0.5	0.18
B-89	45.3	<DL>	128.4	60.65	0.5	<DL>	0.04
Sha-106	54	2.98	212.47	53.88	329.67	<DL>	0.05
Sha-107	86.28	5.18	470.14	65.04	93.2	<DL>	0.06
Sha-108	78.1	3	241.8	137.4	74	<DL>	0.05
Sha-110	77.5	18.33	913.67	70.53	74.33	<DL>	0.05

they were formed at temperatures in the range of 81.8–137.5 °C (Table 1). According to the burial history curve, some of the authigenic quartz was formed at temperatures higher than the normal burial temperature (Fig. 3). In addition, the authigenic quartz with the abnormal formation temperature was formed in the diagenetic fluids with high salinity (Table 1). Al, Ca, and Fe are also included in the quartz overgrowth. This indicates that the authigenic quartz grew continuously and was impacted by the deep fluid in the middle-late Jurassic. The dissolution and alteration of the feldspar and volcanic materials would be the source of the authigenic quartz (Khidir and

Catuneanu, 2003; Xi et al., 2015a, 2015b).

It is well known that in a closed sandstone geochemical system without large-scale advective flow, feldspars and laumontites are generally dissolved and in situ secondary minerals including clays (kaolinite or illite) and quartz cements are precipitated (Giles and De Boer, 1990; Higgs et al., 2007; Yuan et al., 2017). The relationship between the dissolution pores and the kaolinite content are distinct in the Shaqiu area and the Beisantai uplift (Fig. 14). In the Shaqiu area, the kaolinite content is obviously higher than the amount of dissolution pores in feldspar and laumontites. For the minerals with the same volume, anorthite will develop more kaolinites than the K-feldspar, albite, or laumontite. Even if we assume that the dissolved minerals are all anorthites, the kaolinite contents are still higher than the expected amounts (Fig. 14). Therefore, we believe that, in addition to the dissolution of the feldspars and lamontites in the Permian sandstones, the kaolinite can be precipitated by other means. Prior research has shown that the acidic environmental conditions created by hydrothermal actions can promote the alteration of volcanic materials to kaolinites (Karakas and Kadir, 2000; Ece et al., 2003; Kadir et al., 2011, 2014). The underlying Carboniferous strata and Permian formation include abundant andesites, basalts, tuffs, and volcanic debris (Fig. 2). During the middle-late Jurassic, the upwelling of deep fluids into the Permian sandstones promoted the alteration of the volcanic materials in their migration paths and the Permian sandstones. The products would be carried and precipitated in the Permian sandstones. Furthermore, in the Shaqiu area, the kaolinites, were concentrated near the deep fault (Fig. 12B), which indicates that these processes occurred. As described

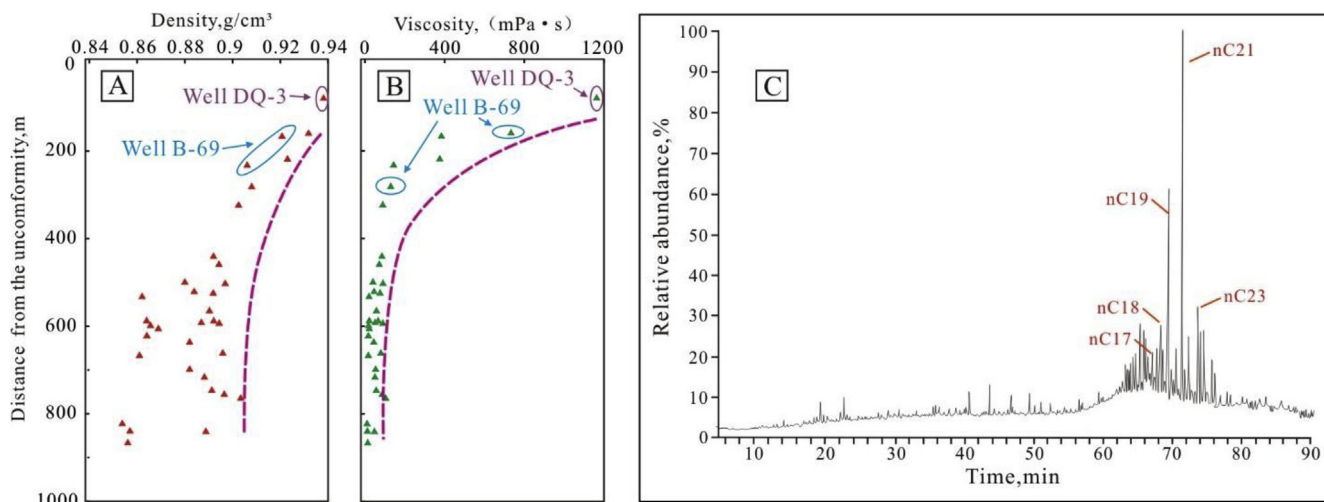


**Fig. 13.** A: The relationship between the crude oil density and the distance from the unconformity. B: The relationship between the crude oil viscosity and the distance from the unconformity. C: The chromatographic analysis of the crude oil in the Permian reservoirs at a depth range of 1534–1600 m in Well DQ-3, which is adjacent to Well B-69.

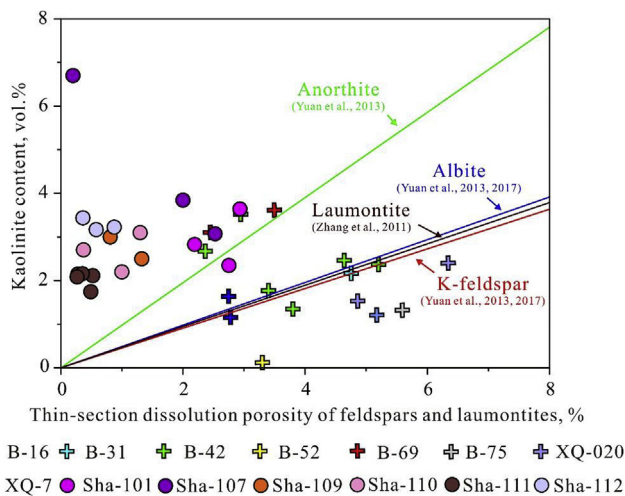


**Fig. 14.** Plot of the amount of dissolution pores in feldspar and laumontite versus the content of kaolinite in thin sections. The brown, green, blue and red lines represent the expected amount of kaolinite formed accompanying dissolution of laumontite, anorthite, albite and K-feldspar in closed geochemical system (Higgs et al., 2007; Zhang et al., 2011; Yuan et al., 2013, 2017). (For interpretation of the references to color in this figure legend, the reader is referred to the Web version of this article.)

above, illites with fibrous and pore-bridging texture would be formed and the illitization of kaolinites would occur at temperatures higher than the normal burial temperatures. This indicates that the illite formation is related to the upwelling of deep fluids in the middle-late Jurassic. Chlorites occur as grain coatings and cling tightly to the grains or mineral surfaces. These chlorite rims would have formed early and were sourced from the hydration of the volcanic materials (Zhu et al., 2016; Cao et al., 2017).

#### 5.4. Meteoric water leaching

The burial history in the study area indicates an intense tectonic uplift during the middle-late Jurassic (Fig. 3). The Permian reservoirs developed in the paleo highland of the Beisantai uplift were eroded during the late Jurassic (Cretaceous strata covers Permian strata directly) (Fig. 1D) and were subjected to meteoric water leaching (Wu et al., 2012). Within a distance of 0–200 m from the unconformity, the content of ( $\text{CO}_3^{2-} + \text{HCO}_3^-$ ) in the pore water is relatively high (Fig. 15A). The unstable minerals, such as feldspars and debris, were intensely dissolved in this depth range (Figs. 9G and 10F). But the authigenic kaolinites were only slightly concentrated in the depth range from 80 m to 120 m (Fig. 15B).

However, in some wells, such as B-75 and B-42, the vertical distance from the Permian sandstones to the unconformity is relatively large. However, if the faults extend up to the unconformity and link to the reservoirs, the meteoric water can likely penetrate into the deep formation (Juhász et al., 2002; Menzies et al., 2014; Yuan et al., 2017). In this situation, the mudstones/shales that are exposed to the meteoric water can be impacted (Falk et al., 2006). Ti and Mn are highly immobile and are easily preserved in mudstones impacted by meteoric water leaching. In contrast, Ca, Cu, Cd, and Zn are relatively soluble and are easily preserved in mudstones that are not impacted by meteoric water leaching. Cr exhibits no differences in these two types of mudstones (Nesbitt and Markovics, 1997; Lavergren et al., 2009). Subsequently, Wu et al. (2003) compared the differences in the elements in mudstones impacted and not impacted by meteoric water leaching in the Wutonggou Formation in the eastern slope of Fukang Sag. The results showed that the mudstones impacted by meteoric water leaching were relatively rich in Ti and contained little or no Ca. The mudstones that were not impacted by meteoric water leaching

contained little or no Ti and had a relatively high Ca content. In the study area, the fracture/fault systems in Beisantai uplift are likely to provide the net channels for the penetrating meteoric water. Hence, we analyzed the trace elements in the mudstone samples from the Wutonggou Formation in the Beisantai uplift and Shaqiu area (Table 4).

According to the differences in the elements, the samples were classified into two groups. The first group includes the mudstones from Well B-12, 16, 20, 21, 52, 55, and 75 in the Beisantai uplift. In these wells, the distance from the Wutonggou Formation to the unconformity is around 200–700 m but the Wutonggou Formation is located in a complex fracture/fault system (Fig. 1C). The second group includes the mudstones from Well Sha-107, 108, and 110 in the Shaqiu area. In these wells, the Wutonggou Formation cannot be linked to the unconformity through the faults (Fig. 1C and D). The mudstones in the first group are impacted by meteoric water leaching (a 0.45% content of Ti and no Ca indicates mudstones impacted by meteoric water leaching in Wu et al. (2003)), while the mudstones in the second group are not impacted by meteoric water leaching (a 2.7% content of Ca and no Ti indicates mudstones not impacted by meteoric water leaching in Wu et al. (2003)). In addition, the mudstones from the first group are relatively rich in Mn. The Cu, Cd, and Zn contents are distinctly lower in the mudstones from the first group, whereas there is no difference in the Cr content between the two groups. These results show that the meteoric water most likely penetrated into the Wutonggou Formation in the Beisantai uplift. However, the Wutonggou Formation developed in the Shaqiu area was not impacted by meteoric water. The meteoric water leaching has caused an intense dissolution of the unstable minerals. For the sandstones from the wells in the first group, the content of secondary pores formed by dissolution is in the range of 2.70–6.99% (average is 4.15%). Additionally, the authigenic kaolinite content is only 0.12–3.3% (average content is 1.56%). In contrast, the secondary pore content only reaches 0.7–4.3% (average content is 1.64%), while the authigenic kaolinite content is in the range of 1.3–6.7% (average content is 3.66%) in the sandstones from the wells in the second group. Compared to the Shaqiu area, the kaolinite content in the Beisantai uplift are obviously less than the amount of dissolution pores in feldspars and laumontites (Fig. 14). Even if we assume that the dissolved minerals are all K-feldspar, most of the kaolinite contents are still close to or lower than the expected amounts. Only a small portion of the products from the dissolution and alteration was preserved in the sandstone geochemical system by kaolinite precipitation in the Beisantai uplift. These results indicate that the sandstone geochemical system is more open in the Beisantai uplift than in the Shaqiu area (Yuan et al., 2017).

#### 5.5. Diagenetic sequences and the impacts of the authigenic minerals on reservoir quality

According to the relationships between the minerals and the minerals and the hydrocarbons, as well as the origins of the authigenic minerals in the Permian sandstones, we established a diagenetic sequence of the Permian sandstones in the study area (Fig. 16). In the Beisantai uplift and the Shaqiu area, the diagenesis has different effects on the reservoir quality. The quantitative statistics indicate that in the Shaqiu area, the laumontite-I (with a range of 4.5–7.4% and an average of 5.5%) and a small amount of quartz in the sandstones developed prior to the middle-late Jurassic. Subsequently, the deep fluid injection dissolved the laumontite-I, feldspar, and debris (with a range of 0.7–4.3% and an average of 1.64%) and then precipitated the kaolinite, quartz, and the subsequent calcites near the faults during the middle-late Jurassic. The illitization could have also occurred during these processes. The kaolinite content was in the range of 1.3–6.7% (average is 3.66%) and the quartz content was in the range of 0.5–2% (average is 0.9%). The content of the calcites ranged from 1% to 17% with an average of 5.7%. After the late Jurassic, the laumontite-II and ferroan calcites were precipitated. These two types of authigenic minerals

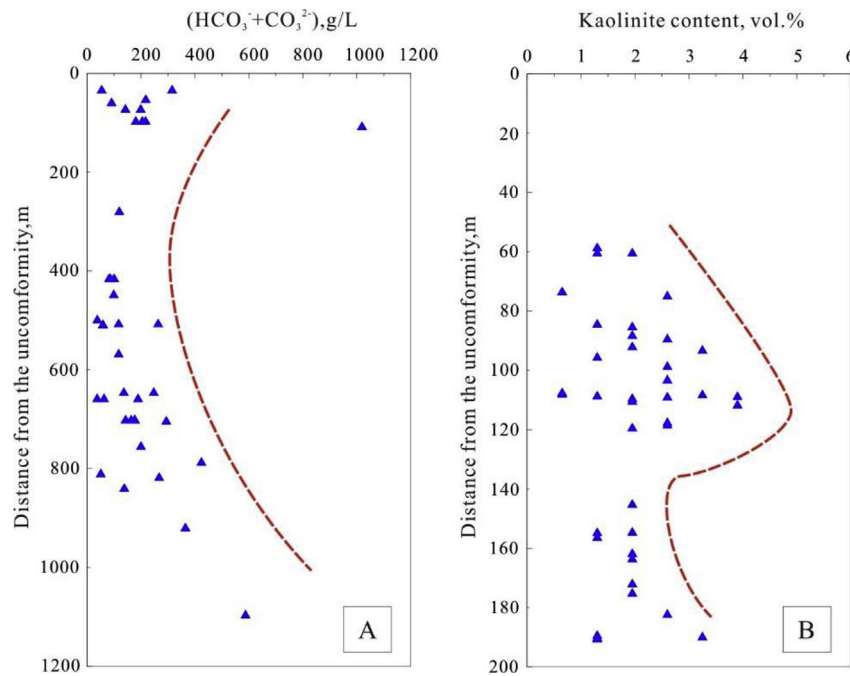


Fig. 15. A: Plots of distance from the unconformity versus the content of  $(\text{HCO}_3^- + \text{CO}_3^{2-})$  in the pore water in the Permian reservoirs. B: Plots of distance from the unconformity versus the kaolinite content in the Permian reservoirs.

reduced the porosity by 2.7–3.5% with an average of 2.9% and 1%–16.5%, respectively. Whereas, in the Beisantai uplift, prior to the late Jurassic, the content of the laumontite-I and calcites was in the range of 6–7.7% with an average of 6.7% and 0.2–15% with an average of 3.66%, respectively. However, except for the dissolution by deep fluids in the middle-late Jurassic, an intense dissolution occurred in the late Jurassic in the Beisantai uplift. A large-scale tectonic uplift resulted in meteoric water leaching in the Beisantai uplift. The secondary pores in the Beisantai uplift were in the range of 2.70–6.99% (average is 4.15%) but the kaolinite content was only 0.12–3.3% (average is 1.56%). After the late Jurassic, the precipitation of the laumontite-II and ferroan calcites reduced the thin-section porosity by 1.9–3.8% with an average of 2.8% and 1–16.5%, respectively. The differences in the contents of the authigenic minerals and the degree of dissolution are important factors resulting in a higher reservoir quality in the Beisantai uplift than in the Shaqiu area (Fig. 4E). Compared to reservoirs experiencing continuous burial processes (Jiang et al., 2015; Li et al., 2015; Cao et al., 2017) in Fukang Sag, reservoirs experiencing a multistage uplift and subsidence possess multistage diagenetic products, such as laumontite-I, laumontite-II, calcite, and ferroan calcite and exhibit multiple dissolutions. During the whole tectonic evolution, the variability of the diagenetic fluids (such as deep fluids or meteoric water) and the diagenetic environment resulted in a relatively complex evolution of the diagenesis and complex reservoir properties.

## 6. Conclusion

- (1) Two types of carbonate cements in the Permian Wutonggou sandstones were identified, including calcites with yellow fluorescent hydrocarbon inclusions and ferroan calcites with blue fluorescent hydrocarbon inclusions. The precipitation of the calcites was related to the upwelling of deep fluids and was impacted by the decarboxylation of organic matters during the middle-late Jurassic. The ferroan calcites in the Beisantai uplift were impacted by the  $\text{CO}_2$  from the biodegradation of crude oil and formed after the late Jurassic.
- (2) Two types of laumontites developed in the Permian sandstones in the study area. The hydration of the volcanic materials was the

primary source of the laumontites. The partially dissolved laumontites were formed prior to hydrocarbon charging and calcite cementation. In contrast, the hardly dissolved laumontites with the hydrocarbon inclusions were formed after hydrocarbon charging and meteoric water leaching.

- (3) Authigenic quartz and kaolinites were formed by the dissolution of feldspars, laumontites, and volcanic materials. Authigenic quartz was formed during or after the oil emplacement but prior to the calcite cementations and was impacted by the deep fluids. Authigenic kaolinites were formed after the dissolution of the feldspars and possess the characteristics of illitization.
- (4) The pore spaces in some of the Permian Wutonggou sandstones close to the deep faults are occupied by calcites. In general, the cementation of calcites reduced more porosity in the Shaqiu area than in the Beisantai uplift. The content of the early laumontites is slightly higher in the Beisantai uplift than in the Shaqiu area. The precipitation of the authigenic quartz has no significant effect on the reservoir quality. The authigenic kaolinites in the Shaqiu area were gathered near the deep faults and reduced a certain amount of pores, whereas reduced a small number of pores in Beisantai area. The early laumontites in the Beisantai uplift were intensely leached by meteoric water during the late Jurassic. The precipitation of the later laumontites and ferroan calcites in the different areas resulted in a small number of pores. The differences in the content of the authigenic minerals and the degree of dissolution are important factors resulting in a higher reservoir quality in the Beisantai uplift than in the Shaqiu area.

## Acknowledgments

This study was supported by the National Science and Technology Major Special Projects (No. 2016ZX05006-003, 2016ZX05006-007), the National Natural Science Foundation of China (No. 41772137, 41702141, U1762217), and the Fundamental Research Funds for the Central Universities (No. 14CX02181A, 17CX05009, 15CX08001A), the National Postdoctoral Program for Innovative Talents (No. BX201600154). We would like to thank the Xinjiang Oilfield Company of PetroChina for providing the related core samples and some



- Bodnar, R.J., 1993. Revised equation and table for determining the freezing point depression of H<sub>2</sub>O-NaCl solutions. *Geochim. Cosmochim. Acta* 57 (3), 683–684.
- Boever, E.D., Muecher, P., Swennen, R., Dimitrov, L., 2011. Evolution of deformation and fault-related fluid flow within an ancient methane seep system (Eocene, Varna, Bulgaria). *Geofluids* 11 (2), 166–183.
- Cao, J., Hu, W.X., Yao, S.P., Zhang, Y.J., Wang, X.L., Zhang, Y.Q., Huang, Z.J., 2007. Carbon, oxygen and strontium isotope composition of calcite veins in the Carboniferous to Permian source rocks of the Junggar Basin: Implications on petroleum fluid migration. *Acta Sedimentol. Sin.* 25 (5), 722–728.
- Cao, B.F., Luo, X.R., Zhang, L.K., Sui, F.G., Lin, H.X., Lei, Y.H., 2017. Diagenetic evolution of deep sandstones and multiple-stage oil entrapment: a case study from the Lower Jurassic Sangonghe Formation in the Fukang Sag, central Junggar Basin (NW China). *J. Petrol. Sci. Eng.* 152, 136–155.
- Carpentier, C., Brigaud, B., Blaise, T., Vincent, B., Durllet, C., et al., 2014. Impact of basin burial and exhumation on Jurassic carbonates diagenesis on both sides of a thick clay barrier (Paris Basin, NE France). *Mar. Petrol. Geol.* 53 (53), 44–70.
- Chen, S.P., Zhang, Y.W., Tang, L.J., 2001. Evolution of Junggar late carboniferous-Permian foreland basin. *J. Univ. Pet., China (Ed. Nat. Sci.)* 25 (5), 11–15.
- Chen, D.Z., Qing, H.R., Chao, Y., 2004. Multistage hydrothermal dolomites in the middle Devonian (givetian) carbonates from the Guilin area, south China. *Sedimentology* 51, 1029–1051.
- Chiper, S.J., Goff, F., Goff, C.J., Fittipaldo, M., 2008. Zeolitization of intracaldera sediments and rhyolitic rocks in the 1.25Ma lake of Valles caldera, New Mexico, USA. *J. Volcanol. Geoth. Res.* 178 (2), 317–330.
- Compton, J.S., 1999. Stable isotope evolution of volcanic ash layers during diagenesis of the miocene Monterey formation, California. *Clay Clay Miner.* 47 (1), 84–95.
- Crossey, L.J., Frost, B.R., Surdam, R.C., 1984. Secondary porosity in laumontite-bearing sandstones: part 2. Aspects of porosity modification. *AAPG (Am. Assoc. Pet. Geol.) Bull.* 59, 225–237.
- Cuadros, J., 1999. Experimental alteration of volcanic tuff: smectite formation and effect on 18O isotope composition. *Clay Clay Miner.* 47 (6), 769–776.
- Drake, H., Tullborg, E.L., Hogmalm, K.J., Astrom, M.E., 2012. Trace metal distribution and isotope variations in low-temperature calcite and groundwater in granitoid fractures down to 1 km depth. *Geochim. Cosmochim. Acta* 84 (3), 217–238.
- Duan, W., Luo, C.F., Lou, Z.H., Liu, J.Z., Jin, A.M., Zhu, R., 2017. Diagenetic differences caused by the charging of natural gases with various compositions - a case study on the lower Zhuhai Formation clastic reservoirs in the WC-A sag, the Pearl River Mouth Basin. *Mar. Petrol. Geol.* 81, 149–168.
- Ece, O.I., Nakagawa, Z., Schroeder, P., 2003. Alteration of volcanic rocks and genesis of kaolin deposits in the site region, northern Istanbul, Turkey. I: Clay Mineralogy: *Clay Minerals* 38 (4), 529–550.
- Ehrenberg, S.N., Nadeau, P.H., 1989. Formation of diagenetic illite in sandstones of the garn formation, Haltenbanken area, mid-Norwegian continental shelf. *Clay Miner.* 24, 233–253.
- Eichhubl, P., Davatzes, N.C., Becker, S.P., 2009. Structural and diagenetic control of fluid migration and cementation along the Moab Fault, Utah. *AAPG (Am. Assoc. Pet. Geol.) Bull.* 93 (5), 653–681.
- Falk, H., Lavergren, U., Bo, B., 2006. Metal mobility in alum shale from Öland, Sweden. *J. Geochem. Explor.* 90 (3), 157–165.
- Folk, R.L., 1980. *Petrology of Sedimentary Rocks*. Hemphill Publications, Austin, Texas.
- Friedman, I., O'Neil, J.R., 1977. Compilation of stable isotope fractionation factors of geochemical interest. In: *Data of Geochemistry*. In: Fleischer, M. (Ed.), Professional Paper: US Geological Survey, sixth ed. pp. 1–12 Washington, DC, USA, 440-KK.
- Fu, G.M., Dong, M.C., Zhang, Z.S., Sun, L., Pan, R., 2010. Formation process and distribution of laumontite in Yanchang 3 reservoir of Fuxian exploration area in north Shaanxi province and the controls of the high quality reservoirs. *Earth Sci. J. China Univ. Geosci.* 35 (1), 107–114.
- Garden, I.R., Guscott, S.C., Burley, S.D., Foxford, K.A., Walsh, J.J., Marshall, J., 2001. An exhumed palaeo-hydrocarbon migration fairway in a faulted carrier system, Entrada Sandstone of SE Utah, USA. *Geofluids* 1 (3), 195–213.
- Gastmans, D., Hutcheon, I., Menegário, A.A., Chang, H.K., 2016. Geochemical evolution of groundwater in a basaltic aquifer based on chemical and stable isotopic data: case study from the Northeastern portion of Serra Geral Aquifer, São Paulo state (Brazil). *J. Hydrol.* 535, 598–611.
- Gaupp, R., Matter, A., Ramseyer, K., Platt, J., Walzebeck, J., 1993. Diagenesis and fluid evolution of deeply buried Permian (rotliegendes) gas-reservoirs, northwest Germany. *AAPG (Am. Assoc. Pet. Geol.) Bull.* 77 (7), 1111–1128.
- Ghent, E.D., Miller, B.E., 1974. Zeolite and clay-carbonate assemblages in the Blairmore group (cretaceous) southern Alberta foothills, Canada. *Contrib. Mineral. Petrol.* 44 (4), 313–329.
- Giles, M.R., De Boer, R.B., 1990. Origin and significance of redistributional secondary porosity. *Mar. Petrol. Geol.* 7 (4), 378–397.
- Glorie, S., Grave, J.D., Buslov, M.M., Elburg, M.A., Stockli, D.F., Van den Haute, P., Gerdes, A., 2010. Multi-method chronometric constraints on the evolution of the northern Kyrgyz Tien Shan granitoids (central Asian orogenic belt): from emplacement to exhumation. *J. Asian Earth Sci.* 38, 131–146.
- Grave, J.D., Buslov, M.M., Van den Haute, P., 2007. Distant effects of India-Eurasia convergence and Mesozoic intracontinental deformation in Central Asia: constraints from apatite fission-track thermochronology. *J. Asian Earth Sci.* 29 (2–3), 188–204.
- Head, I.M., Jones, D.M., Larter, S.R., 2003. Biological activity in the deep subsurface and the origin of heavy oil. *Nature* 426, 344–352.
- Higgs, K.E., Zwingham, H., Reyes, A.G., Funnell, R.H., 2007. Diagenesis, porosity evolution, and petroleum emplacement in tight gas reservoirs, Taranaki Basin, New Zealand. *J. Sediment. Res.* 77 (12), 1003–1025.
- Hoefs, J., 2009. *Stable Isotope Geochemistry*, sixth ed. Springer, Berlin.
- Irwin, H., 1980. Early diagenetic carbonate precipitation and pore fluid migration in the Kimmeridge Clay of Dorset, England. *Sedimentology* 27 (5), 577–591.
- Irwin, H., Curtis, C., Coleman, M., 1977. Isotopic evidence for source of diagenetic carbonates formed during burial of organic-rich sediments. *Nature* 269 (5625), 209–213.
- Jiang, Y.X., Wen, H.G., Zhang, H., Liu, Y.P., Li, Y., Jin, J., 2015. Diagenesis of sandstone reservoirs of qigu formation in fudong slope area, eastern Junggar Basin. *LITHOLOGIC RESERVOIRS* 27 (6), 78–86.
- Jin, B., 2001. Research on the Relationship between the Evolution of Fluid Potential Field and the Distribution of Oil and Gas in the Eastern of Junggar Basin. Master Thesis. China University of Petroleum (Beijing), Beijing, China.
- Jing, X.F., 2009. Research on the Accumulation Conditions and Accumulation Model of the Permian Lithologic Reservoirs in Sha'n'an Area of the Eastern Junggar. Master Thesis. China University of Petroleum (Beijing), Beijing, China.
- Juhász, A., Tóth, T.M., Ramseyer, K., Matter, A., 2002. Connected fluid evolution in fractured crystalline basement and overlying sediments, Pannonian Basin, SE Hungary. *Chem. Geol.* 182 (2), 91–120.
- Kadir, S., Erman, H., Erkoyun, H., 2011. Mineralogical and geochemical characteristics and genesis of hydrothermal kaolinite deposits within Neogene volcanics, Kütahya (western Anatolia), Turkey. *Clay & Clay Minerals* 59 (3), 250–276.
- Kadir, S., Kılıç, T., Eren, M., Önalçıl, N., Gürel, A., 2014. Mineralogical and geochemical characteristics and genesis of the güzeyurt alunite-bearing kaolinite deposit within the late miocene gördeles ignimbrite, central anatolia, Turkey. *Clay & Clay Minerals* 62 (6), 477–499.
- Karakas, Z., Kadir, S., 2000. Devitrification of volcanic glasses in Konya volcanic units, Turkey. *Turkish Journal of Earth Sciences* 9 (1), 39–46.
- Khalifa, M.A., Morad, S., 2012. Impact of structural setting on diagenesis of fluvial and tidal sandstones: the bahi formation, upper cretaceous, NW sirt basin, north Central Libya. *Mar. Petrol. Geol.* 38 (1), 211–231.
- Khidir, A., Catuneanu, O., 2003. Sedimentology and diagenesis of the scollard sandstones in the red deer valley area, central Alberta. *Bull. Can. Petrol. Geol.* 51 (1), 45–69.
- Kim, J.H., Torres, M.E., Haley, B.A., Kastner, M., Pohlman, J.W., Riedel, M., Lee, Y.J., 2012. The effect of diagenesis and fluid migration on rare earth element distribution in pore fluids of the northern Cascadia accretionary margin. *Chem. Geol.* 291, 152–165.
- Labaume, P., Jolivet, M., Souquière, F., Chauvet, A., 2008. Tectonic control on diagenesis in a foreland basin: combined petrologic and thermochronologic approaches in the Grès d'Annot basin (Late Eocene–Early Oligocene, French–Italian external Alps). *Terra. Nova* 20 (2), 95–101.
- Lander, R.H., Bonnell, L.M., 2010. A model for fibrous illite nucleation and growth in sandstones. *AAPG (Am. Assoc. Pet. Geol.) Bull.* 94 (8), 1161–1187.
- Lavergren, U., Astrom, M.E., Bergback, B., Holmstrom, H., 2009. Mobility of trace elements in black shale assessed by leaching tests and sequential chemical extraction. *Geochem. Explor. Environ. Anal.* 9 (1), 71–79.
- Li, Y.J., Zhao, L., Shi, J.A., Zhang, Y., Zou, N.N., 2015. Diagenesis and pore evolution of Jurassic Sangonghe clastic rock formation of fudong slope zone, Junggar Basin. *Natural Gas Geoscience* 26 (s2), 44–51.
- Liu, Z., Jin, B., Han, J., Guan, Q., Li, P.J., 2000. Evolution of fluid potential field in eastern Junggar basin for controlling hydrocarbon migration and accumulation. *Petrol. Explor. Dev.* 27 (4), 59–63.
- Lu, J.G., Chen, S.J., Wang, X.L., Wang, Y., Zhang, J.Z., Shi, Z.H., 2011. Characteristics and origin analysis of viscous oil and reservoir bitumen in Santai-Beisantai area. *Journal of China University of Petroleum* 35 (5), 27–31.
- Macaulay, C.I., Fallick, A.E., Haszeldine, R.S., Macaulay, G.E., 2000. Oil migration makes the difference: regional distribution of carbonate cement δ13C in northern North Sea Tertiary sandstones. *Clay Miner.* 35 (1), 69–76.
- Marantos, I., Markopoulos, T., Christidis, G.E., 2007. Zeolitic alteration in the tertiary ferres volcano-sedimentary basin, Thrace, NE Greece. *Mineral. Mag.* 71 (3), 327–345.
- Marchand, A.M.E., Macaulay, C.I., Haszeldine, R.S., Fallick, A.E., 2002. Pore water evolution in oilfield sandstones: constraints from oxygen isotope microanalyses of quartz cement. *Chem. Geol.* 191 (4), 285–304.
- Menzies, C.D., Teagle, D.A.H., Craw, D., Cox, S.C., Boyce, A.J., Barrie, C.D., Roberts, S., 2014. Incursion of meteoric waters into the ductile regime in an active orogeny. *Earth Planet. Sci. Lett.* 399 (399), 1–13.
- Merino, E., 1975. Diagenesis in Tertiary sandstones from Kettleman North dome, California. I. diagenetic mineralogy. *J. Sediment. Petrol.* 45 (1), 320–336.
- Nesbitt, H.W., Markovics, G., 1997. Weathering of granodioritic crust, long-term storage of elements in weathering profiles, and petrogenesis of siliciclastic sediments. *Geochim. Cosmochim. Acta* 61 (8), 1653–1670.
- Noh, J.H., 1998. Geochemistry and paragenesis of heulandite cements in a Miocene marine fan-delta system of the Pohang basin, Republic of Korea. *Clays and clay mineral* 46 (2), 204–214.
- Noh, J.H., Boles, J.R., 1993. Origin of zeolite cements in the miocene sandstones, north tejon oil fields, California. *J. Sediment. Res.* 63 (2), 248–260.
- Noh, J.H., Lee, I., 1999. Diagenetic pore fluid evolution in the Pohang Miocene sediments: oxygen isotopic evidence of seiparian carbonate concretions and authigenic mineral phases. *Geosci. J.* 3 (3), 141–149.
- Novikov, I.S., 2013. Reconstructing the stages of orogeny around the Junggar basin from the lithostratigraphy of Late Paleozoic, Mesozoic, and Cenozoic sediments. *Russ. Geol. Geophys.* 54 (2), 138–152.
- Pitman, J.K., Goldhaber, M.B., Spoettl, C., 1997. Regional diagenetic patterns in the St. Peter sandstone: implications for brine migration in the Illinois basin. *U.S. Geological Survey Bulletin* 2094-A, 1–15.
- Qiu, N.S., Yang, H.B., Wang, X.L., 2002. Tectono-thermal evolution in the Junggar Basin. *Chinese Journal of Geology* 37 (4), 423–429.
- Rainoldi, A.L., Franchini, M., Beaufort, D., Mozley, P.S., Giusiano, A., Cesaretti, N.N., Patrier, P., Imoicini, A., Pons, J., 2015. Mineral reactions associated with

- hydrocarbon paleomigration in the huincul high, Neuquén Basin, Argentina. *GSA Bulletin* 127 (11/12), 1711–1729.
- Sadegh, J., Hamid, Y., Shahram, M., 2008. Fluid evolution during burial diagenesis and subsequent orogenic uplift: the La Vid group (cantabrian zone, northern Spain). *J. Sediment. Res.* 78 (3–4), 282–300.
- Salem, A.M., Morad, S., Mato, L.F., Al-Aasm, I.S., 2000. Diagenesis and reservoir-quality evolution of fluvial sandstones during progressive burial and uplift: evidence from the upper jurassic boipeba member, recôncavo basin, northeastern Brazil. *AAPG (Am. Assoc. Pet. Geol.) Bull.* 84 (7), 1015–1040.
- Sliwinski, M.G., Kozdon, R., Kitajima, K., Denny, A., Valley, J.W., 2016. Microanalysis of carbonate cement d18O in a CO<sub>2</sub>-storage diagenetic history of the eau claire formation (upper cambrian), Illinois basin. *AAPG (Am. Assoc. Pet. Geol.) Bull.* 100 (6), 1003–1031.
- Suchy, V., Heijlen, W., Sykorova, I., Muech, P., Dobes, P., Hladikova, J., Jackova, I., Safanda, J., Zeman, A., 2000. Geochemical study of calcite veins in the Silurian and Devonian of the Barrandian Basin (Czech Republic): evidence for widespread post-Variscan fluid flow in the central part of the Bohemian Massif. *Sediment. Geol.* 131 (3), 201–219.
- Sugitani, K., Yamashita, F., Nagalka, T., Yamamoto, K., Minami, M., Mimura, K., Suzuki, K., 2006. Geochemistry and sedimentary petrology of Archean clastic sedimentary rocks at Mt. Goldsworthy, Pilbara Craton, Western Australia: evidence for the early evolution of continental crust and hydrothermal alteration. *Precambrian Res.* 147 (1), 124–147.
- Surdam, R.C., Crossey, L.J., 1985. Organic-inorganic reactions during progressive burial: key to porosity/permeability enhancement and/or preservation. *Philosophical Transactions of The Royal Society A Mathematical Physical and Engineering Sciences* 315, 135–156.
- Tang, Z.H., Longstaffe, J.F., Parnell, J., 1997. Diagenesis and reservoir potential of permian-triassic fluvial/lacustrine sandstones in the southern Junggar Basin, north-western China. *AAPG (Am. Assoc. Pet. Geol.) Bull.* 81 (11), 1843–1865.
- Templeton, A.S., Chamberlain, C.P., Koons, P.O., Craw, D., 1998. Stable isotopic evidence for mixing between metamorphic fluids and surface-derived waters during recent uplift of the Southern Alps, New Zealand. *Earth Planet. Sci. Lett.* 154 (1), 73–92.
- Volkman, J.K., Alexander, R., Kagi, R.I., Rowland, S.J., Sheppard, P.N., 1984. Biodegradation of Aromatic Hydrocarbons in Crude Oils from the Barrow Sub-basin of Western Australia, vol. 6. pp. 619–632 (84).
- Wang, M.M., 1992. Formation of oil-gas pools and distribution of oil-gas in the eastern part of Junggar basin. *Petrol. Explor. Dev.* 19 (6), 1–8.
- Wang, Y.Z., Cao, Y.C., Xi, K.L., Song, G.Q., Liu, H.M., 2013. A recovery method for porosity evolution of clastic reservoirs with geological time: a case study from the upper submember of Es4 in the Dongying depression, Jiyang Subbasin. *Acta Pet. Sin.* 24 (6), 1101–1111.
- Wilkinson, M., Haszeldine, R.S., Fallick, A.E., 2014. Authigenic illite within northern and central North Sea oilfield sandstones: evidence for post-growth alteration. *Clay Miner.* 49 (2), 229–246.
- Wopfner, H., Markwort, S., 1991. Early diagenetic laumontite in the lower triassic manda beds of the ruhuhu basin, southern Tanzania. *J. Sediment. Res.* 61 (1), 65–72.
- Wu, K.Y., Zha, M., Hong, M., 2003. Structural models of unconformity and recurrent diagenesis of semi-weathering rock in Junggar basin. *Geotect. Metallogenia* 27 (3), 270–276.
- Wu, X.Z., Zhou, L., Yang, D.S., Qi, X.F., Li, B.H., 2012. Structure evolution and hydrocarbon accumulation the Beisantai uplift in Junggar basin. *Chinese Journal of Geology* 47 (3), 653–668.
- Xi, K.L., Cao, Y.C., Jahren, J., Zhu, R.K., Bjørlykke, K., Zhang, X.X., Cai, L.X., Hellevang, H., 2015a. Quartz cement and its origin in tight sandstone reservoirs of the Cretaceous Quantou formation in the southern Songliao basin, China. *Mar. Petrol. Geol.* 66, 748–763.
- Xi, K.L., Cao, Y.C., Jahren, J., Zhu, R.K., Bjørlykke, K., Haile, B.G., Zheng, L.J., Hellevang, H., 2015b. Diagenesis and reservoir quality of the lower Cretaceous Quantou Formation tight sandstones in the southern Songliao Basin, China. *Sediment. Geol.* 330 (C), 90–107.
- Xi, K.L., Cao, Y.C., Zhu, R.K., Haile, B.G., Hellevang, H., 2016. Evidences of localized CO<sub>2</sub>-induced diagenesis in the cretaceous quantou formation, southern songliao basin, China. *International Journal of Greenhouse Gas Control* 52 (C), 155–174.
- Yang, X.P., Qiu, Y.N., 2002. Formation process and distribution of laumontite in Yanchang formation (Upper Triassic) of Ordos basin. *Acta Sedimentol. Sin.* 20 (4), 628–632.
- Yang, Y., Song, C., He, S., 2015. Jurassic tectonostratigraphic evolution of the Junggar basin, NW China: a record of Mesozoic intraplate deformation in Central Asia. *Tectonics* 34 (1), 86–115.
- Yu, S., Wang, X., Xiang, B., 2014. Organic geochemistry of Carboniferous source rocks and their generated oils from the Eastern Junggar Basin, NW China. *Org. Geochem.* 77, 72–88.
- Yuan, G.H., Cao, Y.C., Xi, K.L., Wang, Y.Z., Li, X.Y., Yang, T., 2013. Feldspar dissolution and its impact on physical properties of Paleogene clastic reservoirs in the northern slope zone of the Dongying sag. *Acta Pet. Sin.* 34 (5), 854–866.
- Yuan, G., Cao, Y., Zhang, Y., Gluyas, J., 2017. Diagenesis and reservoir quality of sandstones with ancient “deep” incursion of meteoric freshwater—An example in the Nanpu Sag, Bohai Bay Basin, East China. *Mar. Petrol. Geol.* 82.
- Zhang, C.J., He, D.F., Wu, X.Z., Shi, X., Luo, J.N., Wang, B.Y., Yang, G., Guan, S.W., Zhao, X., 2006. Formation and evolution of Junggar polycyclic basin. *China Petroleum Exploration* 11 (1), 47–58.
- Zhang, X.H., Huang, S.J., Lan, Y.F., Huang, K.K., Liang, R., 2011. Thermodynamic calculation of laumontite dissolution and its geologic significance. *Lithologic Reservoirs* 23 (2), 64–69.
- Zhong, D.K., Zhou, L.J., Sun, H.T., Yao, J.L., Ma, S.Y., Zhu, H.H., 2012. Influences of petrologic features on diagenesis and pore development: an example from the Triassic Yanchang Formation in Longdong area, Ordos Basin. *Oil Gas Geol.* 33 (6), 890–899.
- Zhou, Y., Ji, Y., Zhang, S., Wan, L., 2016. Controls on reservoir quality of lower cretaceous tight sandstones in the laiyang sag, jiaolai basin, eastern China: integrated sedimentologic, diagenetic and microfracturing data. *Mar. Petrol. Geol.* 76, 26–50.
- Zhu, G.Y., Zhang, S.C., Zhao, W.Z., Wang, Z.J., Liang, Y.B., Zhao, X.F., Zhang, J.Y., 2008. Formation mechanism and geochemical characteristics of shallow natural gas in heavy oil province, China: Science in China Series D. *Earth Sci.* 51 (s1), 96–106.
- Zhu, S.F., Zhu, X.M., Wang, X.L., Liu, Z.Y., 2012. Zeolite diagenesis and its control on petroleum reservoir quality of Permian in northwestern margin of Junggar Basin, China. *Sci. China Earth Sci.* 55 (3), 386–396.
- Zhu, S.F., Zhu, X.M., Liu, X., Wu, D., Zhao, D.N., 2016. Authigenic minerals and diagenetic evolution in altered volcanic materials and their impacts on hydrocarbon reservoirs: evidence from the lower Permian in the northwestern margin of Junggar Basin, China. *Arabian Journal of Geosciences* 9 (2), 1–19.